



POLITECNICO DI TORINO

Master degree course in Aerospace Engineering

Master Degree Thesis

**DNS analysis of warm cloud  
microphysics and related mixing  
dynamic at the cloud-clear air  
interface**

**Supervisor**

Prof.ssa Daniela Tordella

**Candidate**

David CODONI

matricola: 225346

MARCH 2018



# Abstract

A simplified cloud-clear air interface is studied through a direct numerical simulation on a grid of  $512 \times 512 \times 1024$  points. The interface is simulated through a time decaying turbulent shearless mixing layer between two homogeneous and isotropic turbulent field with different turbulent kinetic energy. The Navier-Stokes equations in the Boussinesq approximation are solved for an incompressible fluid together with the advection-diffusion equation for the water vapour density, seen as a passive scalar. Water droplets dynamics is taken into account through the solution of the droplets momentum equations together with the water droplets growth equation. The main water particles growth mechanism are the water vapour diffusional growth and the collision-coalescence growth which are both considered in the code. The feedbacks of the water droplets dynamics on the velocity, temperature and vapour density fields are taken into account. Two simulations has been carried out. The first simulation describes a situation in which the cloud region (the high energy region) is supersaturate and the interface is initially saturate and the Taylor microscale Reynolds number is  $Re_\lambda = 43$ . The second simulation analyse the case in which the cloud region is saturate and the interface is subsaturate, while the Taylor microscale Reynolds number is slightly higher than in the first simulation,  $Re_\lambda = 53$ . In this work not only the main features of the particular turbulent shearless mixing simulated are described but also the temperature and the water vapour density transport across the mixing layer are analysed together with the water droplets dynamics. In particular the role of turbulence in advecting the inertial particles is investigated through the visualization of the clustering phenomenon. The time evolution of the droplets size distribution spectrum has been analysed for both the simulations. The aim of this work is the study of the water droplet dynamic in a saturated and supersaturated turbulent environment and the effect of the entrainment on water droplets at the cloud-clear air interface. In the saturated case, a very strong reduction in the liquid water content due to the intense evaporation is observed, while in the supersaturated case an increase in the liquid water content can be seen. The droplets size distribution analysis showed the

same trend, a strong decrease of the mean droplet radius is observed for the saturated case and a slight increase of the mean radius is seen for the supersaturated case. Finally from the visualization of the water droplets spatial distribution a significant clustering is observed. Furthermore it is shown that the water droplets concentrate in the low vorticity intensity regions. Only two eddy turnover time was simulated and a significant droplet growth cannot be appreciated, but the results obtained agree with the results in literature.

# Acknowledgements

I would like to thank my supervisor Daniela Tordella for her help and scientific guidance. For the code optimization and high performance computing counsel I acknowledge Vittorio Ruggiero of CINECA staff; computational resources were provided by HPC@POLITO, a project of Academic Computing within the Department of Control and Computer Engineering at the Politecnico di Torino (<http://www.hpc.polito.it>); PRACE for awarding us access to the resource Marconi based in Italy at CINECA.

I also thank the PhD students who helped and supported me in this project, Taraprasad Bhowmick and Mina Golshan, and Dott. Federico Fraternali. Finally I want to thank my family for the moral and economic support.

# Contents

<b>1</b>	<b>Introduction</b>	<b>1</b>
<b>2</b>	<b>Warm cloud dynamics</b>	<b>5</b>
2.1	Turbulence role in clouds . . . . .	5
2.2	Cloud-clear air interaction through turbulent transport . . . . .	11
2.2.1	Simplified model of a cloud-clear air interface . . . . .	12
2.2.2	Turbulent shearless mixing in stratified flows . . . . .	18
<b>3</b>	<b>Cloud microphysics</b>	<b>21</b>
3.1	Numerical model for water droplet dynamics simulation . . . . .	25
3.1.1	Collision detection algorithm . . . . .	27
<b>4</b>	<b>Results analysis and conclusion</b>	<b>30</b>
4.1	Water droplets dynamics analysis . . . . .	40
<b>5</b>	<b>Conclusions</b>	<b>60</b>

# Chapter 1

## Introduction

Cumulus convection has a great importance in climate and weather. It plays a key role in the hydrological and energy cycle through the vertical transport of heat, moisture and momentum, it is responsible for precipitation and clouds formation (de Rooy *et al.*, 2013). Atmospheric clouds may extend over distances of several hundred kilometres and among them particular attention is given to "warm" clouds, whose top is below the freezing level. Warm clouds, such as subtropical stratocumulus and tropical shallow cumulus, cover a large portion of Earth's tropic and subtropic and because of that they largely affect the global energy balance through interaction with the incoming solar radiative flux. The solar radiative flux is partitioned into energy reflected back to space (thus contributing to Earth's albedo) and energy absorbed by the climate system (Grabowski & Wang, 2013). Atmospheric aerosol concentration affect the cloud albedo and the cloud lifetime, referred to as the aerosol first and second indirect effects respectively. In particular aerosol number concentration is related to the cloud droplet size distribution and larger droplet and wider droplet size distribution increase the efficiency of the precipitation formation process, thus affecting both aerosol indirect effects (Chandrakar *et al.*, 2016). Furthermore rainfall produced in warm clouds, by a water droplet collision-coalescence growth, accounts for approximately 30% of the total rainfall on the planet and roughly 70% of all rainfall in the Tropics (Lau & Wu, 2003). It is therefore evident the strong impact that this type of atmospheric clouds has on Earth's climate and on climate change.

A warm cloud is a very complex system which involves a wide range of scales, from the cloud microscale (few micrometers) to the global scales (thousands of kilometers). The numerical models used to predict the weather and to study the climate cannot resolve all the scales involved in the system (Grabowski & Wang, 2013). The fact that all these scales are intrinsically linked and the lack of a numerical model that span all the relevant scales make

it difficult to understand this atmospheric phenomenon and particularly to predict cloud lifetime and consequently the development of precipitation (Devenish *et al.*, 2012). In order to get a better understanding on water droplets growing inside a warm cloud and on rain formation, cloud microphysics needs to be studied. For many years a great part of the research has been devoted to understand the microphysical processes inside warm clouds and the role of turbulence on cloud formation, from the cloud scale to the droplet scale. However it is very difficult to make a direct observation and to take a measurement of the cloud microphysical processes, such as cloud droplets nucleation, condensation (evaporation) and collision - coalescence (breakup). In order to study the cloud evolution, the whole process of rain drop formation needs to be described, exploring the continuous growth of droplet from tenth micrometre to hundreds micrometre in radius (Gotoh *et al.*, 2016). Small aerosols (few tenth micrometer) of different nature (e.g. organic material, pollution) dispersed in the atmosphere act as cloud condensation nuclei (CCN). The activation of the CCN due to the supersaturation lead to formation of small water droplet, with a typical radius of about  $1 \mu m$ . These small water droplets, formed from the activated CCN, grow initially by condensation of water vapour. Diffusional growth is the most efficient droplets' growth mechanism by which they reach around  $15 \mu m$  in radius, from the activated CCN size (Beard & Ochs, 1993; Raes, 2006). The rate of increase of droplet radius is inversely proportional to the radius itself. The more the radius increases, the slower it grows until the droplet reaches a size of about  $15 \mu m$ , beyond which water vapour diffusion is no longer an efficient growth mechanism. This inefficiency is due to the fact that the supersaturation decreases during the diffusional growth (Grabowski & Wang, 2013). The collision - coalescence is the main droplet growth mechanism for droplets larger than  $40 \mu m$  in radius. Since both diffusional mechanism and collision - coalescence mechanism are not efficient, it is difficult to explain the rapid cloud droplets growth in the size range  $15 \mu m - 40 \mu m$  in radius, which is called the condensation - coalescence bottleneck or size gap (Grabowski & Wang, 2013).

A fundamental aspect in the study of the clouds dynamics is the role of turbulence and the effects that it has on cloud microphysics. The air turbulence main characteristics are the large Reynolds number, relatively small energy dissipation rates  $\epsilon$ , which ranges from  $10^{-3} m^2 s^{-3}$  in stratocumuli to  $10^{-2} m^2 s^{-3}$  in cumuli (Pruppacher & Klett, 1997), wide inertial subrange and moderate velocity fluctuations (Shaw, 2003). Water droplets are transported and dispersed by the energy containing turbulent eddies (large scale eddies of the order of  $100 m$ ), while they modify the local environment (droplet scale) through the mass, momentum and energy transfers. Furthermore the mass

and energy transfers affect the cloud dynamics through the buoyancy effect. In general the turbulent kinetic energy flows from the cloud scales (around 1  $Km$ ) to dissipative scales (around 1  $mm$ ), while the latent heat flows from the droplet scales to the large cloud scale. For this reason the interaction between the cloud dynamics and cloud microphysics is a very complex multiscale and multiphase phenomenon. Since we focus in cloud microphysics, it is fundamental to investigate the effects that the small scale turbulence has on the droplets growth. The small scale turbulence is described by the Kolmogorov scale which is of the same order of magnitude of the mean distance between droplets, therefore a direct numerical simulation (DNS) is the right approach for this type of study. According to Vaillancourt *et al.* (2002) the small scale turbulence has a negligible effect on droplets growth by condensation due to the fact that the diffusional growth is reversible and a droplet which is growing faster at one instant it will move to a region where the local environment conditions are not conducive to growth. Paoli & Shariff (2009) carried out similar simulations to those of Vaillancourt *et al.* (2002), but they added forcing terms in temperature and moisture equations, obtaining a significant increase in supersaturation field fluctuations. Since these forcing terms are closely related to entrainment (large scale process of bringing unsaturated clear air into the cloud through the instabilities at the cloud - clear air interface) and large scale mixing, Paoli & Shariff (2009) DNS simulations show the great importance of turbulent entrainment, in affecting the droplet spectrum broadening. The small scale turbulence, despite ineffective in the spectral broadening, allows droplet to move from one inertial - range eddy to another. The mechanism through which the small scale eddies and the inertial - range eddies jointly interacts is referred to as large-eddy hopping. The combination of large-eddy hopping mechanism with the energy - containing scale processes, such as entrainment, contributes to a significant spectral broadening. Turbulence largely affect the collision - coalescence mechanism through the enhancement of the collision kernel, defined as the collision rate normalized by the relevant droplet pair concentration. This collision kernel enhancement is a combination of different effects among which the droplet clustering, produced by the small scale turbulence. Finally turbulence seems to play a significant role in accelerating warm rain formation process.

This project focuses on the small - scale microphysical processes and on the study of the dynamics of the interface between a warm cloud and the surrounding clear air. The simulation of the cloud interface and of the cloud microphysics is carried out by a DNS approach. The computational model solves the fluid motion through an Eulerian formulation while the particle motion by a Lagrangian tracking method. The cloud interface is modelled

through two fields at different turbulent kinetic energy, which represent the warm cloud and cloud - free air, respectively. The model solves the equations for the transport of the water vapour and the temperature fields, seen as passive scalars, and it includes a set of equations for the study of the complex cloud droplets dynamics and droplets growth. The diffusional and the collision - coalescence growth mechanisms are taken into account by the computational model, which considers also the droplet's feedback on the fluid. In Chapter 2 a general description of warm cloud physics is presented while particular attention is given to cloud - clear air interface dynamics and its modelling as a turbulent shearless mixing. A description of the model equations implemented in the DNS code is also in this Chapter. In Chapter 3 the focus is on the water droplets dynamics and their growth stages. Results analysis are in Chapter 4 while the final conclusions are in Chapter 5.

# Chapter 2

## Warm cloud dynamics

Atmospheric clouds are the manifestation of the moist convection, which is a mixture of dry air and water vapour. Cloud air is a suspension of moist air and liquid water particles. The clouds which do not contain ice particles but only liquid water, are referred to as "warm clouds", whose cloud-top is below the freezing level. Convective clouds such as cumulus and stratocumulus are examples of warm clouds and they are the two types of clouds on which the present project is focused. The cloud is a very complex atmospheric phenomenon which covers a wide range of scales, from the large scales of the order of magnitude of a  $Km$  till the smallest scale (the Kolmogorov scale) of the order of magnitude of few  $mm$ , and it concerns several different processes, such as entrainment and mixing at the cloud-clear air interfaces, water droplet growth and precipitation. Both the macro- and micro-scale processes are affected by turbulence which plays a key role in the cloud formation and evolution.

### 2.1 Turbulence role in clouds

Convective clouds are multiscale and multiphase turbulent flows. From the fluid dynamics point of view this is due to the fact that the typical Reynolds number of these flows is much higher than the critical Reynolds number which defines the transition to turbulence (from few thousands to tens of thousands). Assuming that typical shallow convective clouds values of velocity and length scales, are around  $1\text{ ms}^{-1}$  and  $100\text{ m}$  and considering the kinematic viscosity of the air, a conservative estimate of the Reynolds number of this type of clouds is of the order of  $10^7$  (Devenish *et al.*, 2012), which guarantees a turbulent flow. As for all the bodies that move in a fluid, even for the Earth a boundary layer develops on its surface. The atmospheric turbulent boundary layer is the

main source of the clouds turbulence, feeding the small convective cumulus updraught. However it is evident that the turbulence intensity is different depending on the cloud type and the level of its evolution. Some estimates of the main parameters which characterize the turbulence in warm clouds, such as the mean turbulent kinetic energy dissipation rate  $\epsilon$  and the Taylor-scale Reynolds number  $R_\lambda$ , are obtained by in-field measurements. Regarding the stratocumulus [Siebert \*et al.\* \(2010\)](#) measured  $\epsilon \sim 1 \text{ cm}^2\text{s}^{-3}$  and obtained  $R_\lambda \sim 5000$ , while for the small cumulus clouds [Siebert \*et al.\* \(2006\)](#) measured  $\epsilon \sim 10 \text{ cm}^2\text{s}^{-3}$  with  $R_\lambda$  between  $\sim 30000$  and  $40000$ . These estimates are only mean values and they do not provide any information about the large fluctuations in the local dissipation rate. The dissipation rate  $\epsilon$  seems to vary with height, in particular from the cumulus clouds measurements performed by [MacPherson & Isaac \(1977\)](#) and [Gerber \*et al.\* \(2008\)](#) it is shown that  $\epsilon$  reach the maximum near the cloud top. Furthermore, the turbulence intensity is the highest near the cloud edge because of the turbulent entrainment and mixing between the cloudy and the environment air ([Siebert \*et al.\*, 2006](#)), while it is much smaller below the cloud base. Entrainment plays a key role in the clouds dynamics. It occurs when two turbulent fluids with different densities penetrate each other and then mixes. The entrainment is a three-stages process. Firstly, it takes place the engulfment of dry air of the surrounding environment by turbulent cloudy air. Through the action of turbulence, the engulfment forms filaments of dry and cloudy air and as these filaments reach the Kolmogorov scale, the mixing process acts to obtain a homogeneous mixture of the two different fluids ([Devenish \*et al.\*, 2012](#)). The entrainment process depends on the environmental conditions and on the cloud type. In isolated cumulus, dry air entrainment causes a strong cloud dilution compared to its effects on a stratocumulus. For cumulus clouds the nature of the entrainment is still subject of debate. While [Squires \(1958\)](#) argues that vertical entrainment, through the penetrative downdraught into the cloud top, was the main dilution mechanism in cumulus clouds, [Blyth \*et al.\* \(1988\)](#) states that cloud top entrainment, considering the small descending mass fluxes, cannot cause the observed dilution in cumulus clouds. More recent results obtained by [Heus \*et al.\* \(2008\)](#) showed that lateral entrainment is the primary dilution mechanism. [Heus & Jonker \(2008\)](#) developed a conceptual view in which the cumulus convection was modelled through a cloud core, with positive buoyancy, surrounded by a descending shell negatively buoyant, originated by evaporative cooling. Dry air is so entrained through the descending shell and the mixing between dry and cloudy air is not instantaneous. These results agree with the observations. Stratocumulus dynamics is very different from the dynamics of the isolated cumulus clouds and so the entrainment processes are different. Stratocumulus

forms at the stably stratified transition layer (temperature inversion or density interface) which separates the shallow, cool and moist thermal boundary layer and the much warmer and drier subsiding atmosphere, capping the mixing layer. In this case the entrainment of warm and dry air from above occurs at the cloud top interface, thanks to the convective turbulence, driven by infrared radiative cooling at the cloud top, impacting the cloud top interface (Stevens, 2005). The mixture resulting from the mixing between the warmer subsaturated air above the temperature inversion and the saturated cooler air below it, can be negatively buoyant. The buoyancy is a non-linear function of the fraction of the two fluids involved in the mixing (see 2.1). During the

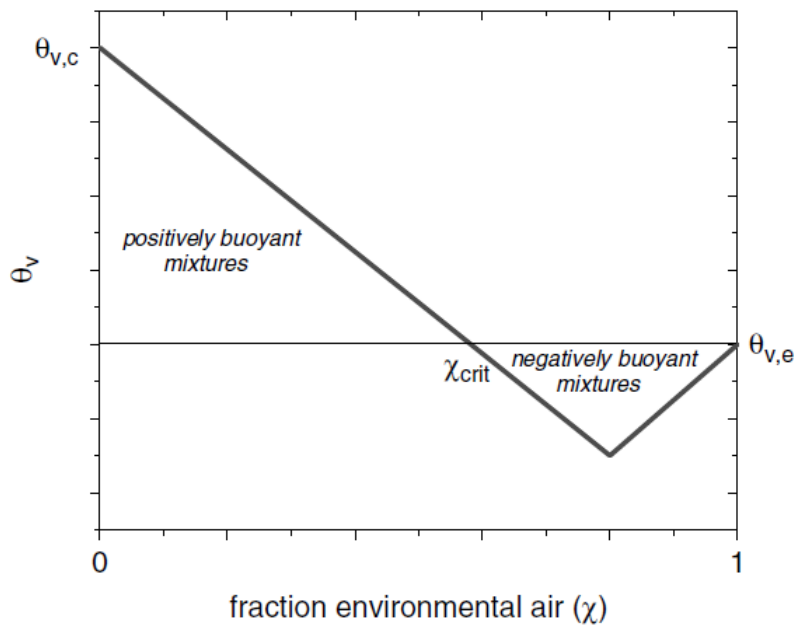


Figure 2.1. The virtual potential temperature  $\theta_v$  (a measure of density) of the cloudy-clear air mixture is a function of the fraction of the environmental air ( $\chi$ ) in the mixture. The value  $\chi_{crit}$  is the limit of  $\chi$  to which the mixture is neutrally buoyant. The values  $\theta_{v,c}$  and  $\theta_{v,e}$  are the virtual potential temperature of the cloudy air ( $\chi = 0$ ) and of the environmental air ( $\chi = 1$ ) respectively (de Rooy *et al.*, 2013).

mixing the subsaturated air dilutes the saturated air causing the water droplet to evaporate and if the temperature of the mixture is not sufficient to offset the evaporating cooling, the density of the mixture will be higher than both the two mixing fluids. This phenomenon is known as the buoyancy reversal and

it causes dry air mass fluxes to penetrate the cloud top. Buoyancy reversal can lead to the cloud top entrainment instability but it is not sufficient to destabilize stratocumulus. Aircraft measurements (Gerber *et al.* (2005)) confirm the existence of an entrainment interfacial layer, a mixture with a particular fraction of the mixed fluids that does not lead to negative buoyancy. As a result there is not a direct mixing between cloudy and dry air, but a mixing occurs between the entrainment interfacial layer and the cloud top. The entrainment rate is modified by the presence of this layer. This layer is not deep so its dynamics is governed by the small scale turbulence and so the entrainment is not only an energy-containing eddies process but it is also sensitive to the smaller scales. As already mentioned in Chapter 1, after the cloud condensation nuclei activation, the cloud droplets grow by molecular diffusion and condensation of water vapour until they reach a size of around  $15 \mu m$  in radius. Water droplets larger than  $50 \mu m$  grow efficiently by collision and coalescence, while droplet growth in the size range of  $15 - 50 \mu m$  still remains difficult to explain. Turbulence and gravity have a great effect on the droplet growth mechanism and consequently on the droplet size distribution. The droplet are assumed to be spherical and any droplet shape deformation is neglected. Moreover since we are interested in the effect of turbulence on the growing of the particles, we focus on small droplets with a radius of less than  $100 \mu m$ . For small droplets the Reynolds number, calculated using as reference quantities the velocity of the particle relative to the flow and particle diameter, is small enough that the Stokes law is used as a good approximation. According to the Stokes drag, the inertial response time of the droplet  $\tau_p$  is

$$\tau_p = \frac{2}{9} \frac{\rho_w a^2}{\mu}$$

where  $\rho_w$  is the water density and  $\mu$  is the air dynamic viscosity. Since the typical value of the Kolmogorov length scale for small cumulus cloud is  $\eta \approx 1 mm$  (Shaw, 2003) and it is much larger than the droplet size, we deduce that the small-scale turbulence dynamics is very important, particularly the dissipation range. The interactions between turbulence, gravity and water particles are characterized by two important parameters, the Stokes number  $St$  and the non-dimensional parameter  $Sv$ . The number of Stokes is defined as the ratio of the droplet inertial response time to the Kolmogorov time scale  $\tau_\eta$

$$St = \frac{\tau_p}{\tau_\eta}$$

If the Stokes number is large (more than 1) so it is the particle inertia and the droplet and the fluid motions are likely to be uncorrelated. The  $Sv$  parameter

is defined as the ratio of the eddy turnover time (in the dissipation range this time is the Kolmogorov time scale) to the time that it takes for a droplet to sediment across that eddy  $\tau_v$

$$Sv = \frac{\bar{\tau}_\eta}{\tau_v}$$

or in velocity terms

$$Sv = \frac{v_T}{v_\eta}$$

where  $v_T$  is the terminal velocity and according to the Stokes drag hypothesis it is defined as  $v_T = \tau_p g$ . Finally if  $St$  represents the particle inertial response to the turbulent changes, the  $Sv$  quantifies the relative importance of gravity (sedimentation) and turbulence. Since

$$\tau_\eta = \left(\frac{\nu}{\epsilon}\right)^{1/2} \text{ and } v_\eta = (\epsilon\nu)^{1/4}$$

it follows that

$$St \sim \epsilon^{1/2} \quad Sv \sim \epsilon^{-1/4}$$

where  $\epsilon$  is the energy dissipation rate. Both  $St$  and  $Sv$  depend on  $\epsilon$  but the gravity and turbulence effect on microphysics cannot be fully described by the variation of these two parameters with the mean values of  $\epsilon$ . The energy dissipation rate has a distribution of values. There are localized region in which the dissipation rate assumes values very different from the mean value due to the fluctuations. Droplet growth by condensation of water vapour depends on the ambient condition, that is the temperature and moisture fields in the vicinity of a droplet. From a time scale analysis [Vaillancourt \*et al.\* \(2001\)](#) shows that the ratio of the slowest time scale associated with the water droplet growth by condensation, to the fastest time scale relative to the ambient conditions changes due to turbulence, is less than one. For this reason the temperature and moisture fields can be assumed to be steady-state fields. The condensational growth of particles is strictly related to the supersaturation field  $s$ . The supersaturation, which is defined as  $s = e/e_s - 1$  where  $e$  and  $e_s$  are the actual and saturated vapour pressure, is affected by the vertical velocity fluctuations and the spatial droplet distribution. In the past decades extensive research has been carried out to better understand the effects of small-scale turbulence and sedimentation on droplet spectrum broadening and on the condensational growth. [Vaillancourt \*et al.\* \(2001\)](#) showed that a random spatial droplet distribution, neglecting the sedimentation effect, significantly perturbs the supersaturation field. The small scale turbulence affect the droplet distribution (clustering). [Shaw \*et al.\* \(1998\)](#) showed the effect of droplet clustering

on the condensational growth. The authors assert that fluctuations in droplet concentration due to turbulence cause large fluctuations in supersaturation  $s$ . In this case single droplets grow at different rates according to their position in the flow, provoking the broadening of the droplet size spectrum. According to [Vaillancourt \*et al.\* \(2002\)](#), who studied particle condensational growth in a homogeneous isotropic turbulent field, sedimentation reduces the widening of the droplet spectrum. Moreover the authors argued that increasing the dissipation rate  $\epsilon$  leads to an increase of the supersaturation fluctuations due to droplet clustering, but the supersaturation fluctuations and droplets are less correlated. The small-scale turbulence alone does not explain the observed broadening of the droplet spectrum. In conclusion [Sidin \*et al.\* \(2009\)](#) simulated a wider range of scales through the use of a kinematic simulation. They studied the condensational growth and they assert that both large and small-scale turbulence are necessary to reach a significantly broadening of particle spectrum. According to the large-eddy hopping mechanism (see [Chapter 1](#)) droplets move from one large-eddy to another through the action of the small scales, which mix droplets of different growth history. The large-eddies have different vertical velocity and consequently they may have different levels of supersaturation  $s_{eq}$ , where  $s_{eq}$  is the supersaturation at the equilibrium. Cloud droplets grow at different rates in different large-eddies, while the small-scales mix them and so the droplet size spectrum widens. The collision-coalescence is the main growth mechanism for larger droplets and it is governed by geometric collisions, collision efficiency and coalescence efficiency. In this project it is assumed that the coalescence always occurs whenever a collision occurs. The assumption is justified for droplets smaller than  $100 \mu m$  as shown in wind tunnel experiments conducted by [Vohl \*et al.\* \(1999\)](#). Turbulence affect the collision kernel, which is a measure of the collision rate, through the increase of the droplet relative velocity and the enhancement of the radial distribution function (RDF). In the case of a monodisperse distribution, when the number of Stokes is low there is a strong correlation between droplet velocities and the fluid and consequently droplets relative velocity is low and turbulence is not so efficient in enhancing the collision rate. Things are different when  $St$  is larger and approach the unity, in this situation a high decorrelation induces an increase in the relative velocity. For bidisperse droplet gravity produce an efficient increase in particle relative velocity. Small-scale turbulence is also responsible for the droplet clustering producing strong inhomogeneities in their spatial distribution, enhancing the RDF and consequently the collision rate. Particularly the droplets move towards region of low vorticity and high strain rate due to centrifugal effect ([Maxey, 1987](#)). In conclusion turbulence inertial effects, such as clustering, can accelerate the droplet growth in the size gap.

Moreover turbulence effects, enhancing the collision kernel, lead to an important acceleration in the warm rain formation (Grabowski & Wang, 2013).

## 2.2 Cloud-clear air interaction through turbulent transport

It is not an easy task to study the dynamics of the interface between cloudy air and environmental air, because of the many processes that occur at the cloud's interfaces, such as entrainment and mixing, latent heat flows, buoyancy effects. The structure of the interface depends on the type of clouds (the stratocumulus top interface is different from the small cumulus top) and also on what kind of interface is being considered, if it is an isolated small cumulus lateral edge interface or its top/bottom interface. At the lateral edge interface of an isolated small cumulus cloud, entrainment and mixing between cloudy and clear air are not instantaneous and they happen through the descending shell, which is a negatively buoyant flow originated from evaporative cooling. Many research campaign has been carried out in order to understand the cloud top interface dynamics. In situ high spatial resolution measurements of temperature and liquid water content, together with modest humidity and turbulent fluctuations measurements, have been collected by Malinowski *et al.* (2013) during the stratocumulus top campaign. The authors proposed a division into layer of the stratocumulus top region. In the figure 2.2 the temperature, liquid water content and velocity fluctuations profiles allow us to recognize the distinctive features of the layers. Proceeding downward from above the cloud top (in the figure 2.2 from left to right), the first region is the free troposphere *FT*, characterized by small velocity fluctuations and small temperature gradient and by the absence of liquid water. Then at a certain altitude the temperature drops about 8 K. Temperature and velocity fluctuations increase while the liquid water content is still zero, suggesting the presence of a layer between the cloud top and the *FT*, the so called turbulent inversion sublayer *TISL* (67728–67735 s in fig. 2.2). Just below this layer, the authors identified a region characterized by peaks in the *LWC* alternate with null value part, indicating that the aircraft penetrated a series of cloudy and clear air filaments. This region, where temperature and velocity fluctuations are increased, is named cloud top mixing sublayer *CTMSL* (67735–67750 s in fig. 2.2). The *CTMSL* and the *TISL* together form the entrainment interfacial layer *EIL*, through which occur the mixing between the cloudy and the environmental air. Finally the aircraft reach the cloud top layer *CTL*, just below the *EIL*. In the *CTL*, the *LWC* fluctuates in a considerable way and it takes everywhere positive

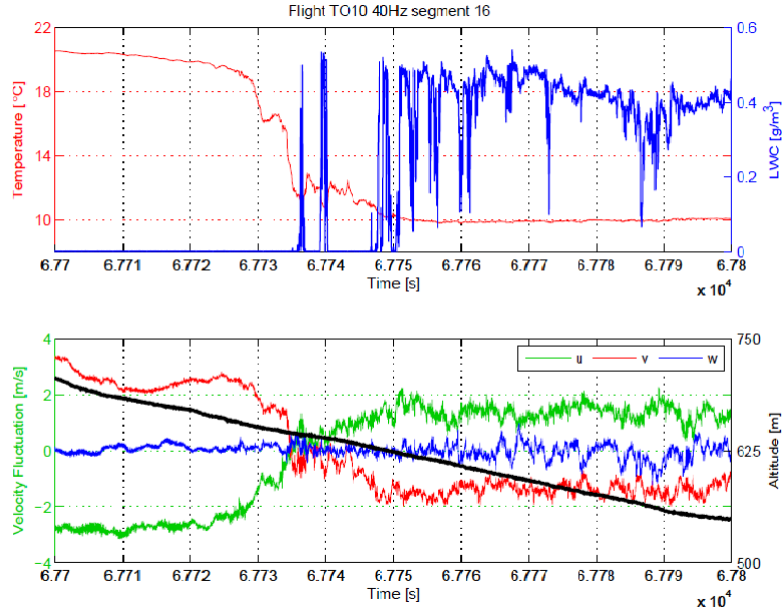


Figure 2.2. In the top panel it is shown the temperature  $T$  and liquid water content  $LWC$  profiles during the aircraft descent into the stratocumulus from the free troposphere above the cloud top. In the bottom panel velocity fluctuations and the altitude profiles are illustrated (Malinowski *et al.*, 2013).

values, the temperature fluctuations become very small, while the velocity fluctuations are significantly large, particularly the vertical component. In figure 2.3 it is illustrated the variation across the layers of the turbulent kinetic energy and of the gradient of the liquid potential temperature  $\theta_l$ , which is defined as

$$\theta_l = \theta \exp \frac{-q_l L_v}{c_p T} \quad \text{with } \theta = T \frac{\pi}{p} R / c_p$$

where  $\theta$  is the potential temperature, which is constant with the pressure for isentropic displacement,  $\pi$  is the reference pressure,  $q_l$  is the liquid water mixing ratio,  $L_v$  is the latent heat of evaporation and  $c_p$  is the constant pressure specific heat (Stevens, 2005).

### 2.2.1 Simplified model of a cloud-clear air interface

In the present work the cloud-clear air interface dynamics and microphysics are studied. The simulations are performed through a DNS (Direct Numerical Simulation) code which implements a pseudospectral Fourier-Galerkin spatial discretization and an explicit fourth order low storage Runge-Kutta time integration scheme. The convective term is computed through the 3/2 de-aliased

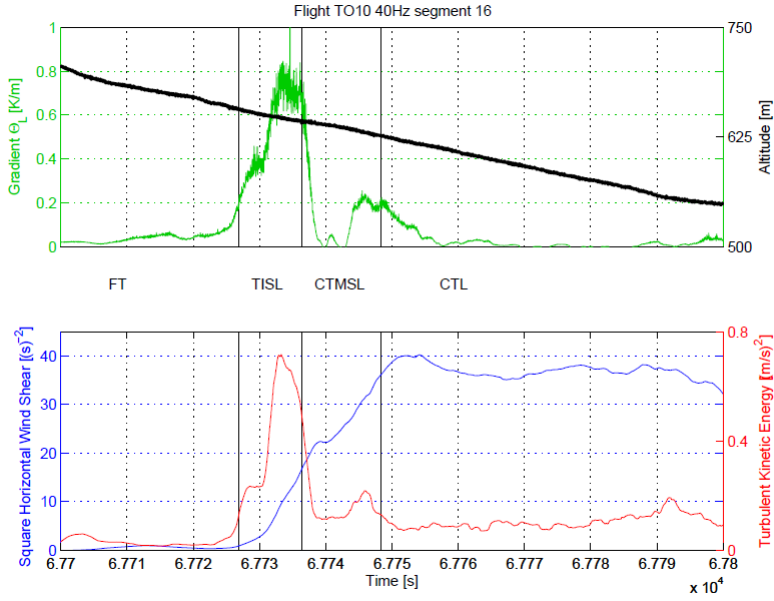


Figure 2.3. In the top panel it is represented the gradient of the liquid water potential temperature  $\theta_l$  in the cloud top, cloud mixing, inversion and in the free troposphere, while in the bottom panel horizontal wind and turbulent kinetic energy are illustrated for the same layers (Malinowski *et al.*, 2013).

method (Iovieno *et al.*, 2001). The code uses a slab parallelization (only one direction of the computational domain is distributed among the processors) and the MPI (Message Passing Interface) standard was adopted. A small portion of the atmosphere in-between a warm cloud and the clear air above, is simulated in a parallelepiped domain. The cloud-clear air interface is modelled as a turbulent shearless mixing in stratified condition. The turbulent shearless mixing is generated by joining two homogeneous and isotropic turbulent field with different turbulent kinetic energy, but with the same integral scale (see figure 2.4). The highest turbulent kinetic energy region simulates the warm cloud, while the other region simulates the environmental air above the cloud top. Periodic boundary conditions in the three directions are considered. The two turbulent homogeneous regions are randomly generated according to the physical conditions imposed by the user, that are the energy spectrum, the integral scale, solenoidality and the kinetic energy. The initial velocity field is obtained by a linear matching of the two homogeneous and isotropic regions with different kinetic energy, which interact through a mixing layer, whose initial thickness is almost equal to the integral scale  $l$  of the simulation we want to make. The aim of the simulation is to study the microphysics of a warm cloud

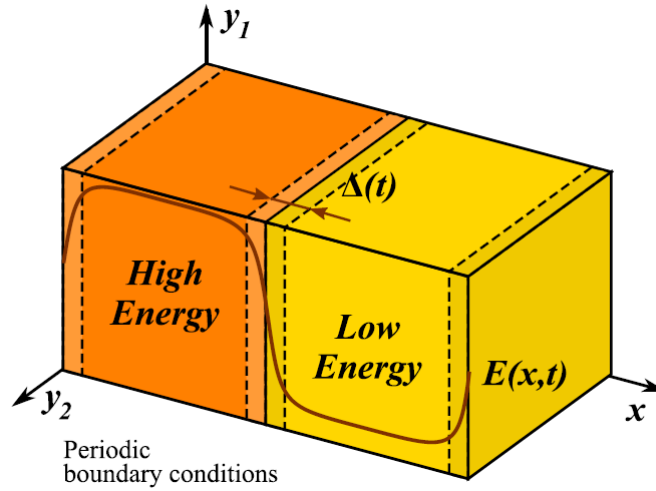


Figure 2.4. The parallelepiped domain obtained by joining two cubes in which are defined two turbulent homogeneous and isotropic field with different kinetic energy is illustrated.  $\Delta$  is the initial mixing layer thickness. Periodic boundary conditions are considered (Tordella & Iovieno, 2011).

top interface, for this reason only the small scales of the turbulence are solved, as it is shown in figure 2.5 which illustrates the wave-number range simulated. The fluid motion is computed through an Eulerian formulation together with the humidity and the temperature fields, seen as passive scalars. The water droplets dynamics are also taken into account. A Lagrangian tracking method is used to calculate the particle motion and an additional equation for the particle size variation is also solved. The simulation describes the water droplets growth taking into account the condensation/evaporation processes and the collision and coalescence mechanism. A particular module implemented in the DNS code is able to detect the collision between particles and it is assumed that every collision leads to coalescence. The droplet equations and a more detailed discussion about water particle dynamics is described in Chapter 3. The Navier-Stokes equations for an incompressible fluid are solved applying the Boussinesq approximation, as the buoyancy effect and the temperature variations need to be taken into account. In general, temperature variations can be introduced through temperature differences at the boundaries or they can be produced by release of latent heat associated to the water evaporation/condensation. In the present simulation a local perturbation  $\theta'$  of the standard atmospheric temperature profile has been implemented. The temperature and the water vapour fields are imposed as initial conditions in all the domain according to the profiles shown in figure 2.6 and 2.7. These tem-

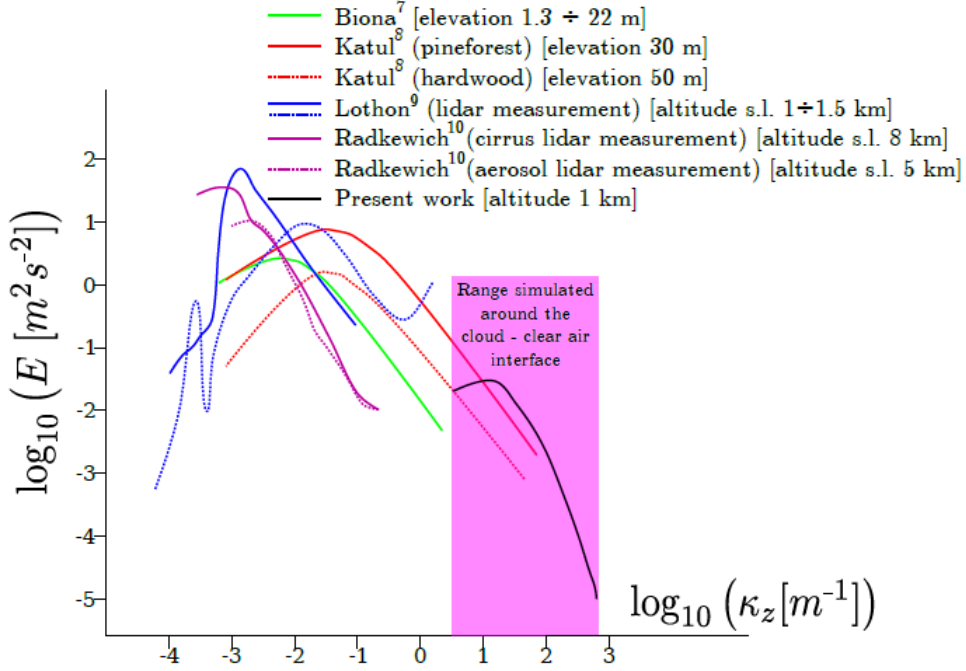


Figure 2.5. Kinetic energy spectra from in situ atmospheric observations are illustrated in coloured lines, while the black solid line shows the present simulation energy spectrum which covers the smallest scales of the inertial range and the dissipative range (Gallana *et al.*, 2014).

perature variations lead to fluid properties variations, such as heat capacity, density and viscosity. According to the Boussinesq approximation (Tritton, 1988) all fluid properties variations are neglected except for the density. In particular density,  $\rho$ , is assumed to be constant except when its variations,  $\Delta\rho$ , give rise to the gravitational force, a body force which is named the buoyancy force. This approximation is justified by the fact that  $\Delta\rho/\rho \ll 1$  and that the flow accelerations are small compared to the gravity acceleration  $g$ . The Navier-Stokes equations for an incompressible fluid in the Boussinesq approximation, coupled with the advection-diffusion equation for the water vapour density  $\rho_v$  (seen as a passive scalar), are shown below

$$\nabla \cdot \mathbf{u} = 0 \quad (2.1)$$

$$\frac{\partial \mathbf{u}}{\partial t} + \mathbf{u} \cdot \nabla \mathbf{u} = -\frac{1}{\rho_0} \nabla p + \nu \nabla^2 \mathbf{u} - Bg + f_p \quad (2.2)$$

$$\frac{\partial T}{\partial t} + \mathbf{u} \cdot \nabla T = k \nabla^2 T - \frac{L}{c_p} C_d \quad (2.3)$$

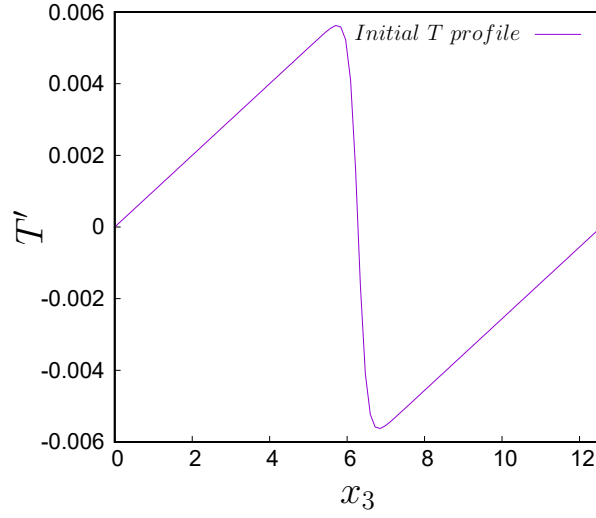


Figure 2.6. Initial temperature profile.

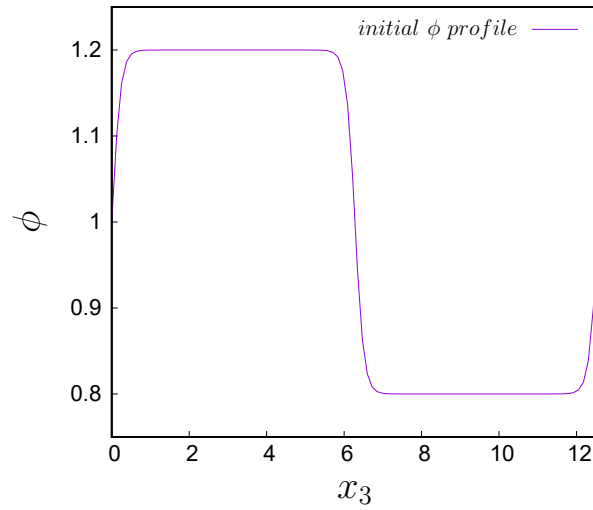


Figure 2.7. Initial density profile.

$$\frac{\partial q_v}{\partial t} + u \cdot \nabla q_v = k_v \nabla^2 q_v - C_d \quad (2.4)$$

where 2.1 is the continuity equation, 2.2 is the momentum equation, while 2.3 and 2.4 are the advection-diffusion equations for the temperature and water vapour density. In 2.4 the variable  $q_v$  is the water vapour mixing ratio and it is defined as  $q_v = \rho_v / \rho_0$ , where  $\rho_0$  is the dry air density at the initial temperature

$T_0$ . The term  $B\mathbf{g}$  in the equation 2.2 is the buoyancy force, with

$$B = \frac{T - T_0}{T_0} + \frac{M_v}{M_a} \frac{\rho_v - \rho_{v0}}{\rho_{v0}}$$

where  $\rho_{v0} = \rho_{vs}(T_0)$  is the saturated water vapour density at  $T_0$  and  $M_v/M_a$  is the ratio of water molar mass to dry air molar mass. In the equation 2.3,  $L$  is the latent heat of evaporation/condensation,  $c_p$  is the constant pressure specific heat,  $k$  is air thermal diffusivity while  $k_v$  is the vapour diffusivity. The terms  $f_p$  and  $C_d$  are the particle force per unit volume on the fluid phase and the condensation rate per unit volume respectively and they represent the water droplet momentum and mass feedback on the fluid flow, in particular

$$f_p = -\frac{1}{\rho_0 V} \sum_k m_k \frac{dv_k}{dt} \quad (2.5)$$

$$C_v = \frac{1}{V} \sum_k \frac{dm_k}{dt} \quad (2.6)$$

where the summation index  $k$  is referred to all the particles in the computational grid cell,  $V$  is the computational grid cell volume,  $m_k$  is the single particle mass and  $v_k$  is the droplet velocity. In the code non-dimensional equations are solved, for this reason all variables must be dimensionless. In order to make them dimensionless, the model reference quantities has to be introduced. The reference length is  $L_R$ , the velocity reference is the initial velocity root mean square  $U_R$ , the ambient conditions  $T_0$ ,  $p_0$  and  $\rho_0$  are the reference quantities for temperature and pressure, while the saturated water vapour density at  $T_0$  is the reference quantity for water vapour density. The dimensionless variables are defined as follow

$$\tilde{x} = \frac{x}{L_R} \quad \tilde{u} = \frac{u}{U_R} \quad \tilde{T} = \frac{T - T_0}{T_0}$$

$$\tilde{p} = \frac{p - p_0}{\rho_0 U_R^2} \quad \tilde{R} = \frac{R}{L_R} \quad \tilde{\rho}_v = \frac{\rho_v}{\rho_{v0}}$$

Finally dimensionless parameters are defined as

$$Re = \frac{U_R L_R}{\nu} \quad Pr = \frac{\nu}{k} \quad Sc_v = \frac{\nu}{k_v}$$

$$\alpha_F = \frac{g L_R}{U_R^2}$$

where  $Re$  is the Reynolds number and  $Pr$  is the Prandtl number. Finally the dimensionless set of the Navier-Stokes equations for the fluid phase in the Boussinesq approximation are obtained

$$\nabla \cdot u = 0 \quad (2.7)$$

$$\frac{\partial u}{\partial t} + u \cdot \nabla u = -\nabla p + \frac{1}{Re} \nabla^2 u - \alpha_F B + f_p \quad (2.8)$$

$$\frac{\partial T}{\partial t} + u \cdot \nabla T = \frac{1}{RePr} \nabla^2 T - \frac{\rho_w}{\rho_0} \frac{L}{c_p T_0} C_d \quad (2.9)$$

$$\frac{\partial \rho_v}{\partial t} + u \cdot \nabla \rho_v = \frac{1}{ReSc} \nabla^2 \rho_v - \frac{\rho_w}{\rho_{v0}} C_d \quad (2.10)$$

where  $B = \tilde{T} + \tilde{\rho}_v - 1$  and  $\alpha_F B$  is proportional to  $N_{ci}^2 = g\alpha dT/dz$  which is the characteristic Brunt-Väisälä frequency of initial condition, where  $\alpha$  is the fluid thermal expansion coefficient and  $z$  is the vertical direction. The Froude number  $Fr$  is the dimensionless parameter defined as the ratio of the inertial to buoyancy forces and it is  $Fr = \frac{u_{rms}}{N_{ci} l}$  where  $l$  is the simulation integral scale (Gallana *et al.*, 2014). In conclusion the buoyancy term in the equation 2.8 is proportional to the inverse of Froude to the square  $\alpha_F B \sim 1/Fr^2$ . High values of Froude number mean negligible stratification while low values of Froude mean strong stratification.

## 2.2.2 Turbulent shearless mixing in stratified flows

The turbulent shearless mixing layer is the simplest example of inhomogeneous turbulent flow. In the present work a turbulent shearless mixing layer is obtained through the interaction of two homogeneous and isotropic turbulent field (HIT), which have different kinetic energy (Tordella *et al.*, 2008). In this kind of mixing a mean flow is not considered and consequently there is no production of turbulent kinetic energy and no mean advective transport. The initial velocity conditions  $u$  for the inhomogeneous field is obtained by matching the two turbulent velocity fields,  $u_1$  and  $u_2$ , through a hyperbolic tangent function (Tordella *et al.*, 2008)

$$u(x) = u_1(x)p(x) + u_2(x)(1 - p(x))$$

with

$$p(x) = \frac{1}{2} \left[ 1 + \tanh \left( a \frac{x}{L} \right) \tanh \left( a \frac{x - L/2}{L} \right) \tanh \left( a \frac{x - L}{L} \right) \right]$$

where  $x$  is the inhomogeneous direction,  $L$  is the length of the computational domain in the  $x$  direction and  $a$  is a coefficient that defines the initial mixing layer thickness. The coefficient  $a$  has a particular value so that the initial mixing layer thickness is of the same order of the integral length scale. The velocity field of the higher turbulent kinetic energy region,  $u_1$ , is obtained by defining the initial energy spectrum, while the lower energy region velocity field,  $u_2$ , is obtained by simply multiplying the velocity field  $u_1$  by a constant. In this project the constant value has been chosen in such a way that the initial energy ratio between the two HIT fields is  $E_1/E_2 = 6.7$  which is consistent with the cloud top measurements obtained by Malinowski *et al.* (2013) (see figure 2.3). The integral length scale does not depend on the turbulent energy intensity, but only on how the energy is distributed among the wavenumbers, in particular the small wavenumbers that depend on the boundary conditions and they do not have universal behaviour (Tordella & Iovieno, 2006). Based on how the lower energy velocity field was built, the two HIT field have the same energy spectrum and consequently the turbulent shearless mixing layer temporal evolution is only driven by the energy gradient, while the integral length scale is homogeneous throughout the field. Due to the lack of forcing terms in the momentum equations, only a decaying turbulent mixing is considered. As said in the previous section, a small temperature perturbation across the mixing layer (see figure 2.6) is considered, through which fluid density variations are taken into account. In this work, the turbulent shearless mixing layer of a stratified flow is analysed. A stratified flow is a flow mainly in the horizontal direction affected by vertical density variations. Density may decrease with height, giving rise to a stable stratification, or it may increase, leading to an unstable stratification (Tritton, 1988). The Froude number  $Fr$  is a dimensionless parameter, defined as the ratio of the inertial forces to the buoyancy forces due to density variations, which gives information on the intensity of the stratification. For low  $Fr$  values, the flow is strongly stratified and vertical fluid motions are strongly damped, while for high  $Fr$  values the stratification is weak. In the simulations we have carried out, the Froude number is low and its squared value is negative and consequently the stratification is strong and unstable (see figure 2.8).

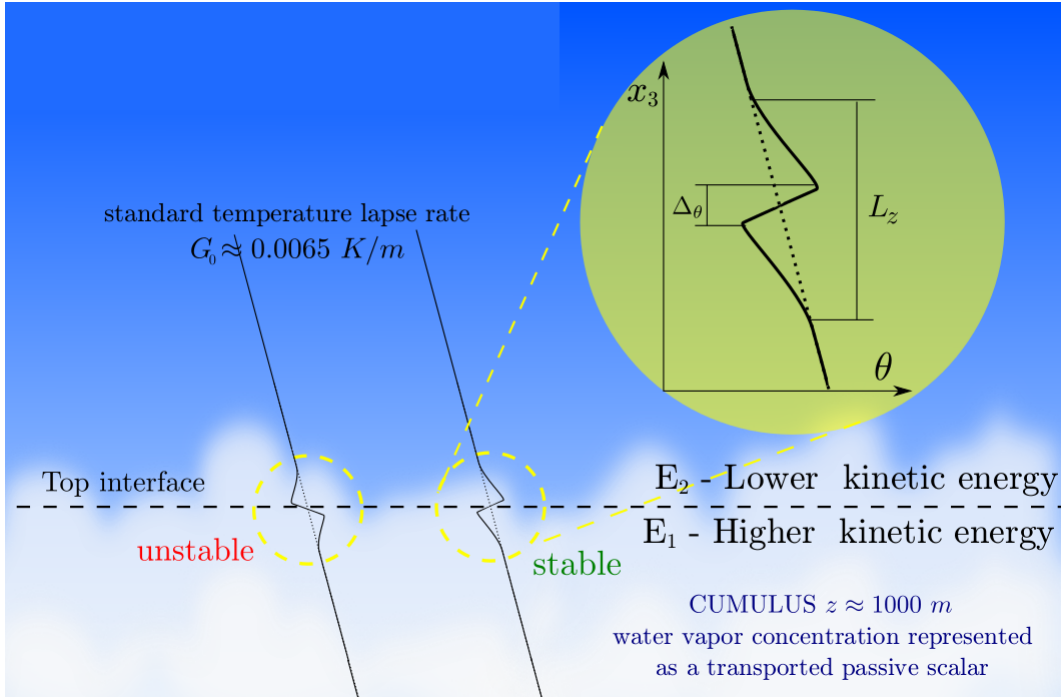


Figure 2.8. The cartoon shows the initial temperature perturbation at the cloud top interface under stable and unstable stratification.  $E_1$  is the mean turbulent kinetic energy of the cloud region, while  $E_2$  is the mean kinetic energy in the cloud free air region. In this work the initial energy gradient is  $E_1/E_2 = 6.7$ . In the circle it is represented an example of the temperature perturbation for the stable stratification case.  $\Delta\theta \approx 0.12 \text{ m}$  is the initial mixing layer thickness (Gallana *et al.*, 2014).

# Chapter 3

## Cloud microphysics

The study of the cloud microphysics concerns the analysis of the whole water droplets dynamics, from the particle advection by small and large scale turbulence to the evolution of the water droplet size distribution spectrum. The role of turbulence on droplet growth was discussed in Chapter 2. The water droplets growth is a complex process characterized by different stages: the activation of CCN (Cloud Condensation Nuclei), diffusional growth, collision and coalescence growth till the raindrops' formation. The small aerosol particles, dispersed in the atmosphere, indirectly affect the optical properties of the warm clouds. Albedo and cloud lifetime depend on the aerosol concentration, which has a strong influence on the droplet size distribution, affecting the droplets' concentration and mean radius. The experiments carried out by Chandrakar *et al.* (2016) show that a decrease of the aerosol concentration leads to the broadening of the droplet size distribution (see figure 3.1). According to the authors, the broadening is due to the large supersaturation fluctuations which occur for low aerosol concentration, when the system is in the regime of slow microphysics. The slow microphysics regime is the limiting regime where the phase relaxation time  $\tau_c$  is greater than the turbulence correlation time  $\tau_t$  (Chandrakar *et al.*, 2016). The atmospheric aerosols act like cloud condensation nuclei, CCN, and are responsible for the droplet formation. Near the cloud base, where the relative humidity crosses the saturation, first the largest CCN are activated and then, as the supersaturation continues to increase, the smaller CCN activation occurs. After that a sufficient number of CCN are activated, the supersaturation starts to decrease due to the fact that already activated droplets begin to grow, and the CCN activation stage is complete. The activated cloud condensation nuclei are small droplets of around  $1 \mu m$  of radius. The small water droplets initially grow by diffusion and condensation of water vapour. The diffusional growth is a very efficient growth mechanism for droplet of less than  $20 \mu m$  in radius. The rate

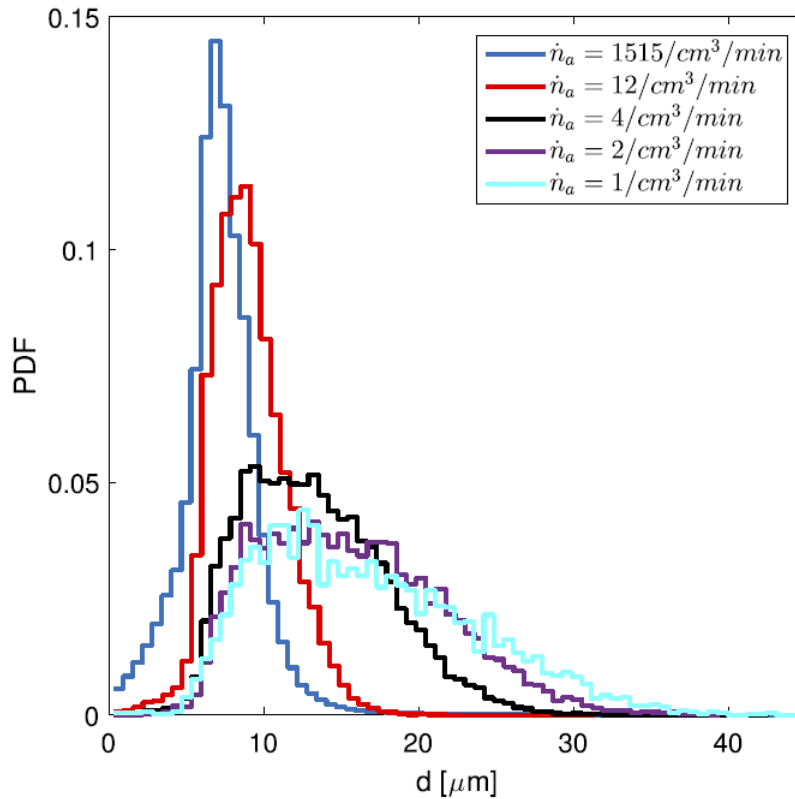


Figure 3.1. The figure shows the probability density function of the cloud droplet diameter for five different aerosol concentrations. The aerosol concentration is represented in terms of aerosol injection rates, which are the aerosol concentration divided by the chamber volume and multiplied by the injection flow rate. It is evident the change in shape of the PDFs, in particular the broadening of the PDFs as the aerosol number concentration increases (Chandrakar *et al.*, 2016).

of increase of the water particle radius is inversely proportional to the radius itself, so the larger droplets grow slower than the smaller ones (Grabowski & Wang, 2013). The water droplet growth by gravitational collision and coalescence is very effective when the particles reach at least  $40 \mu\text{m}$  in radius (Pruppacher & Klett, 1997). Since the collision kernel (i.e. the normalized collision rate) depends on the water droplet relative velocity, the collisions between droplets are enhanced by gravity when droplets of different sizes are in the cloud. In case a monodisperse droplet distribution is considered, the turbulent collision occurs. The droplets clustering (preferential concentration) is due to the turbulent transport of the inertial particles by the small scale

turbulence. [Vaillancourt \*et al.\* \(2002\)](#) argue that turbulence has a negligible effect on the droplets diffusional growth, due to the particles positions rapid rearrangement according to which the fast growing droplets move to regions where the water vapour condensation is inhibited by the low level of supersaturation. Figures 3.2 and 3.3 show the clustering of droplets of different sizes related to the vorticity field. It is evident that water droplets move to regions with low vorticity intensity. In the collision-coalescence process, in-

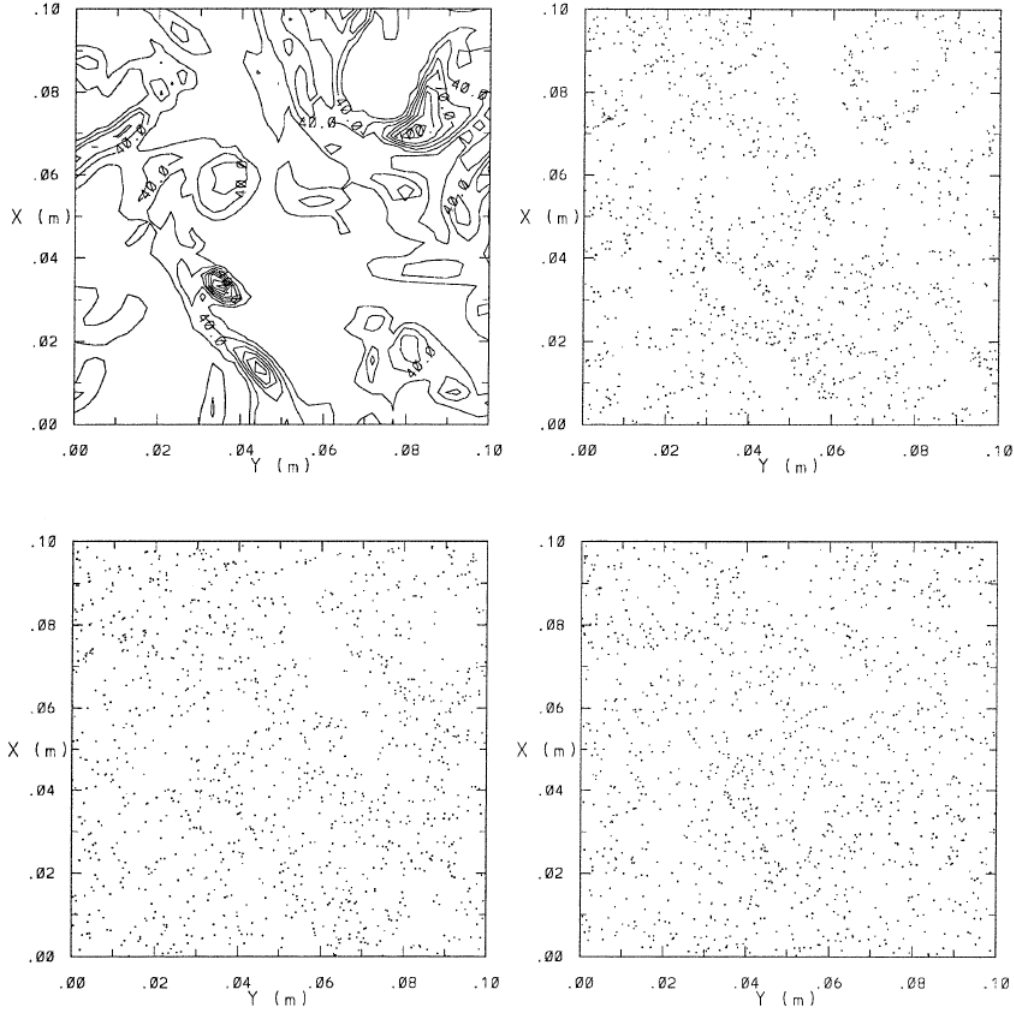


Figure 3.2. In the top left panel the cross section of the vorticity intensity field is represented, in the top right panel the positions of droplets of  $20 \mu\text{m}$  in radius is shown for the same cross section, in the bottom left  $15 \mu\text{m}$  and in the bottom right  $10 \mu\text{m}$  droplets positions are shown ([Vaillancourt \*et al.\*, 2002](#)).

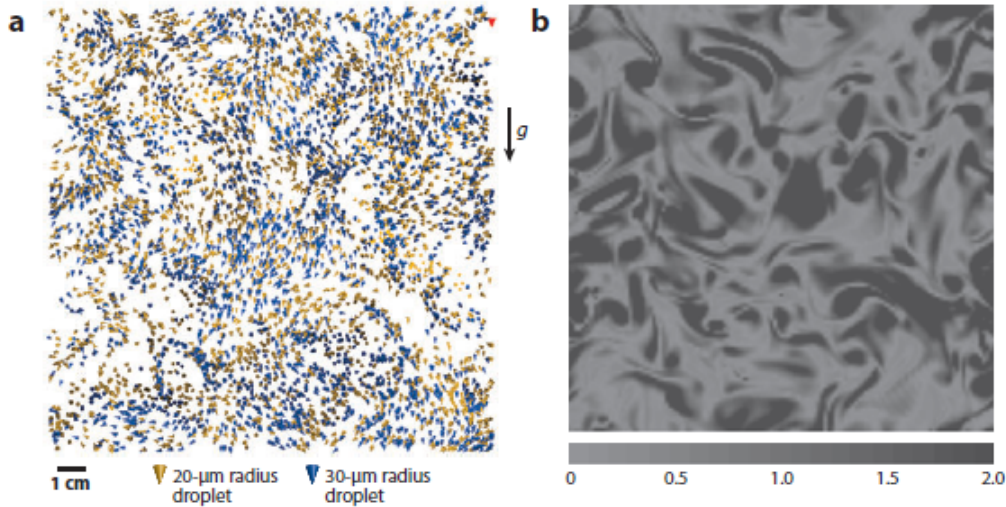


Figure 3.3. The left panel shows the positions of droplets of two different sizes: 20  $\mu\text{m}$  and 30  $\mu\text{m}$  in radius. The 20  $\mu\text{m}$  droplets show a weaker clustering than the 30  $\mu\text{m}$  droplets. The right panel illustrates the normalized flow enstrophy the same planar section (Grabowski & Wang, 2013).

interactions between droplets, called hydrodynamic interactions, play a key role especially for smaller particles (less than 60  $\mu\text{m}$ ) whose inertial response time is very short. When two droplets of different size approach each other viscosity causes the smaller particle to be deflected from the collision trajectory. This deflection is less intense for increasing droplet inertia (Devenish *et al.*, 2012). In this project all droplet-droplet interactions are neglected, consequently particles trajectories are not affected by the presence of the other particles and every collision leads to coalescence of droplets. The water droplets growth in the size range between 15  $\mu\text{m}$  and 40  $\mu\text{m}$  in radius, is still matter of debate and it is difficult to explain, since both the diffusional and the collision-coalescence growth mechanisms are ineffective in that particular size range, which is called the condensation-coalescence bottleneck or the size gap. The effects of turbulent mixing and entrainment, between cloudy and clear air, on the cloud microphysics was studied by Kumar *et al.* (2013) through direct numerical simulations which couple an Eulerian description of the turbulent velocity and water vapour fields with Lagrangian tracking of cloud water droplets. Particularly interesting is the evolution of the droplet size distribution during the turbulent entrainment process for two different cases. In the first case (see left panel of figure 3.4) the vapour content relaxes to a homogeneous field below the saturation level and all droplets evaporate. In the second case (see right

panel of figure 3.4) the water vapour fluctuations decay to zero but the vapour content relaxes to the saturation value leaving a distribution of droplets with a mean radius  $r_\infty$  at the steady state. In both cases the droplet size distribution is negatively skewed due to the particles non-uniform exposure to the subsaturated air. In conclusion, turbulence plays a key role in accelerating in a significant way the process of warm rain formation (Grabowski & Wang, 2013).

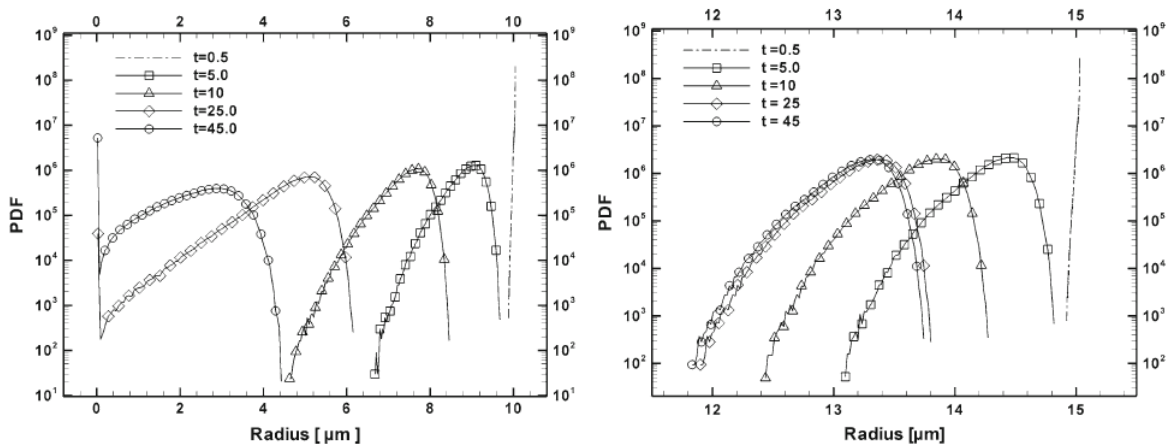


Figure 3.4. The figure shows the time evolution of the droplet radius PDF during the turbulent entrainment process. In the left panel the time evolution of droplet radius PDF is shown for an initial radius  $R_0 = 10 \mu m$  (case 1) and for  $R_0 = 15 \mu m$  (case 2) in the right panel. Data for  $R_\lambda = 59$ ,  $N_{drop} = 1100000$  and  $N_x^3 = 256^3$  (Kumar *et al.*, 2013).

### 3.1 Numerical model for water droplet dynamics simulation

As already mentioned in Chapter 2, the DNS code used to carry out the simulations of this project, solves the Navier-Stokes equations in the Boussinesq approximation for an incompressible fluid together with the water vapour density advection-diffusion equation. This code also contains a module for the Lagrangian tracking of water droplets. The module tracks the motion of each particle through the solution of the related momentum equations, according to the Stokes drag approximation and considering gravity. The equations for water droplets positions and velocities are

$$\frac{dx_k}{dt} = v_k \quad (3.1)$$

$$\frac{dv_k}{dt} = \frac{u(x_k, t) - v_k}{\tau_p} + g \quad (3.2)$$

where  $x_k$  is the droplet position,  $v_k$  is its velocity while  $u$  is the fluid velocity in the droplet position. Furthermore the water droplets dynamics model implemented in the code takes into account the condensation and evaporation processes and the related latent heat release. The droplets are assumed to be spherical. The water droplets radius,  $R_k$ , is considered to vary as a function of the local relative humidity  $\phi$  in correspondence of the droplet position. According to the model developed by [Vaillancourt \*et al.\* \(2001\)](#) for the droplet dynamics, the droplet growth equation is

$$R_k \frac{dR_k}{dt} = KS \quad (3.3)$$

with

$$S = \frac{p}{p_{sat}(T)} - 1 = \frac{\rho_v}{\rho_{vs}(T)} - 1 \quad K^{-1} = \frac{\rho_w R_v T}{p_{sat}(T) D_v} + \frac{L \rho_w}{\rho_a c_p k_a T} \left( \frac{L}{T R_v} - 1 \right) \quad (3.4)$$

where  $S$  is the supersaturation defined in terms of the water vapour pressure  $p$  and the saturated water vapour pressure at the temperature  $T$ ,  $p_{sat}(T)$ , or in terms of vapour density  $\rho_v$  and saturated vapour density  $\rho_{vs}(T)$ . Then  $\rho_w$  and  $\rho_a$  are the water and dry air density respectively,  $R_v = 461.5 \text{ J/KgK}$  is the gas constant for water vapour,  $D_v$  is the water vapour diffusivity,  $k_a$  is the thermal diffusivity,  $c_p$  is the constant pressure specific heat and  $L$  is the latent heat of condensation/evaporation. Two important non-dimensional parameter provide insights into the relative importance of the thermal and vapour diffusivity respect to the momentum diffusivity of air and they are the Prandtl number  $Pr = \nu/k_a \approx 0.71$  and the Schmidt number  $Sc = \nu/D_v \approx 0.61$ . In the code the equation implemented is slightly different, the last term  $\left( \frac{L}{T R_v} - 1 \right)$  is simply written as  $\frac{L}{T R_v}$ , and the supersaturation is defined in terms of water vapour density. The final form of the droplet radius equation is obtained substituting  $K$  and  $S$  in the equation [3.3](#)

$$\frac{dR_k}{dt} = C \frac{\phi(x_k, t) - 1}{R_k} \quad (3.5)$$

with

$$C = \left[ \rho_w \left( \frac{R_v T}{D_v p_{sat}(T)} + \frac{L^2}{\rho_a c_p k_a R_v T^2} \right) \right]^{-1}$$

where  $\phi = \rho_v/\rho_{vs}(T)$  is the relative humidity. The water vapour saturation pressure  $p_{sat}$  is approximated by the Clapeyron-Clausius law

$$\log \frac{p_{sat}}{p_R} = \frac{L}{R_v} \left( \frac{1}{T_R} - \frac{1}{T} \right)$$

where the subscript "R" indicates a reference quantity. Since the code solves non-dimensional equations, using the same reference quantities and non-dimensional parameters described in Chapter 2, we make the equations 3.5 non-dimensional

$$\frac{d\tilde{R}}{d\tilde{t}} = \frac{1}{ReSc_r} \frac{1}{R_{in}^2} \frac{\rho_{vs}(T_0)}{\rho_w} \left( \tilde{\rho}_v - \frac{\exp\left(\frac{L}{R_v T_0} \frac{\tilde{T}}{1 + \tilde{T}}\right)}{1 + \tilde{T}} \right) \frac{1}{\tilde{R}} \quad (3.6)$$

where  $Re$  is the Reynolds number,  $Sc_r = \nu/D_{v_{mod}}$  is the modified Schmidt number (obtained using the modified vapour diffusivity  $D_{v_{mod}}$ ) and  $R_{in}$  is the non-dimensional initial radius of the initial droplet monodisperse spatial distribution, which is used to normalized the droplet radius. In addition droplets can collide. The collision between water particles is taken into account by a module that check at each time step the occurrence of collisions. As already said in this Chapter introduction, droplet-droplet interactions are not considered and if the distance between two droplets centres is less than the sum of their respective radii, a collision between them is supposed to happen.

### 3.1.1 Collision detection algorithm

In order to reduce the number of operations to detect the droplets collisions, the domain is divided into smaller portions (subvolumes) that contain fewer particles. The collision detection algorithm is organized in four stages. Firstly the domain of each core is divided in cells. The grey area in figure 3.5 is the part of domain assigned to the core  $P_i$ , while the thick black line define the regions distributed to different cores. In each cell the algorithm looks for binary collisions, but at this stage only the pairs inside the cells are detected (blue dots in figure 3.5) but not the pairs whose particles belong to different cells (red dots in figure 3.5). The partition of the domain is shifted by half cell in one direction, the green lines in figure 3.6 show the original domain partition, before the shift. After the shift all the pair that were at the borders of the previous cells are now inside the shifted cells and can be detected. If the shift direction is distributed, this step requires the transfer of particles (pink dots in figure 3.6) between the adjacent cores (from core  $i + 1$  to  $i$  and from core  $i$  to  $i - 1$ ). The third stage is the same of the first one except that now

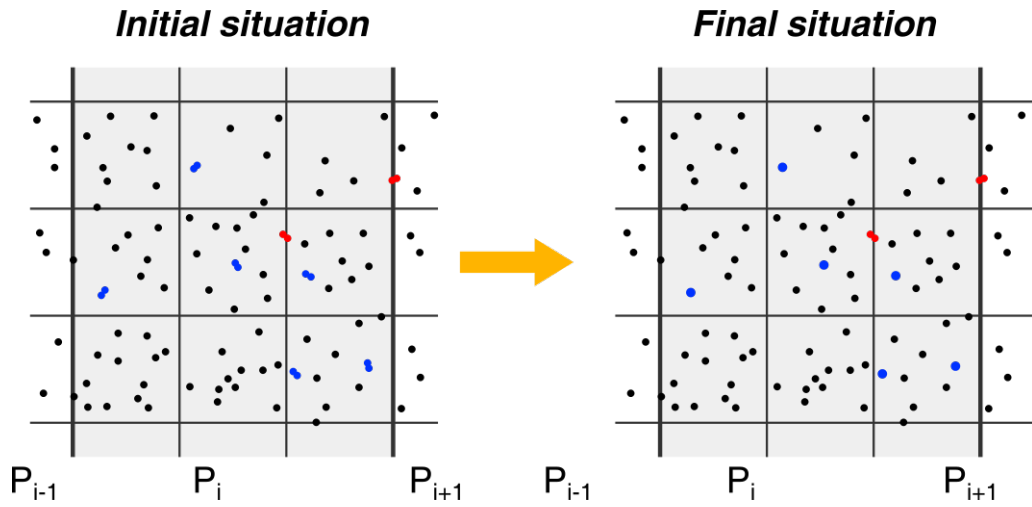


Figure 3.5. First collision detection (PHILOFLUID, 2016).

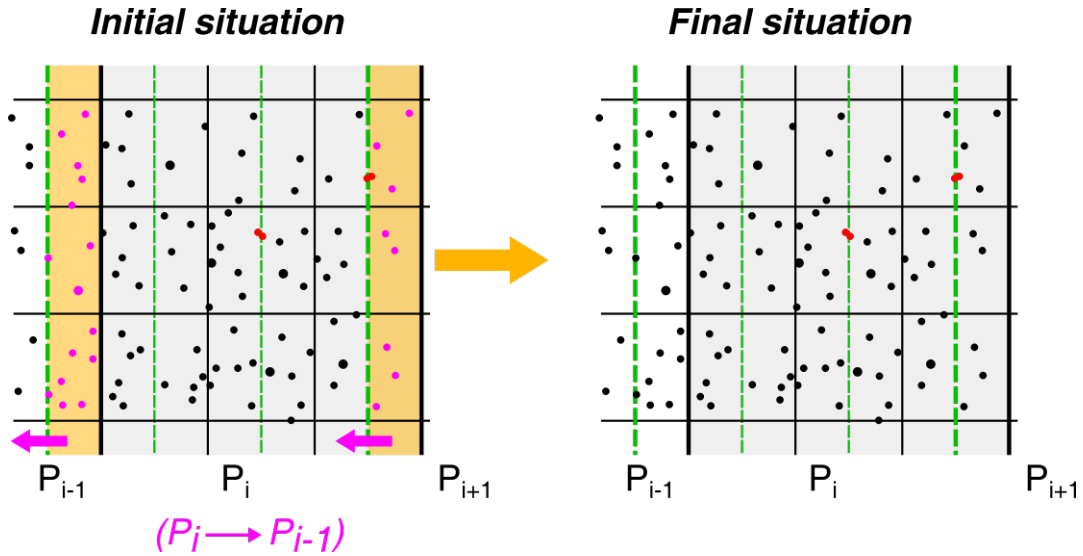


Figure 3.6. Particle transfer through the domain partition shift (PHILOFLUID, 2016).

the collisions detection is carried out on the shifted cells (see figure 3.7). In the last stage (see figure 3.8) the domain partition is shifted again by half cell, but in the opposite direction as compared to the second step, and the original domain distribution among the cores is restored. Cores communications occurs if the direction is distributed (from core  $i - 1$  to  $i$  and from core  $i$  to  $i + 1$ ). The steps 2 – 4 need to be repeated for each spatial direction. Detection of

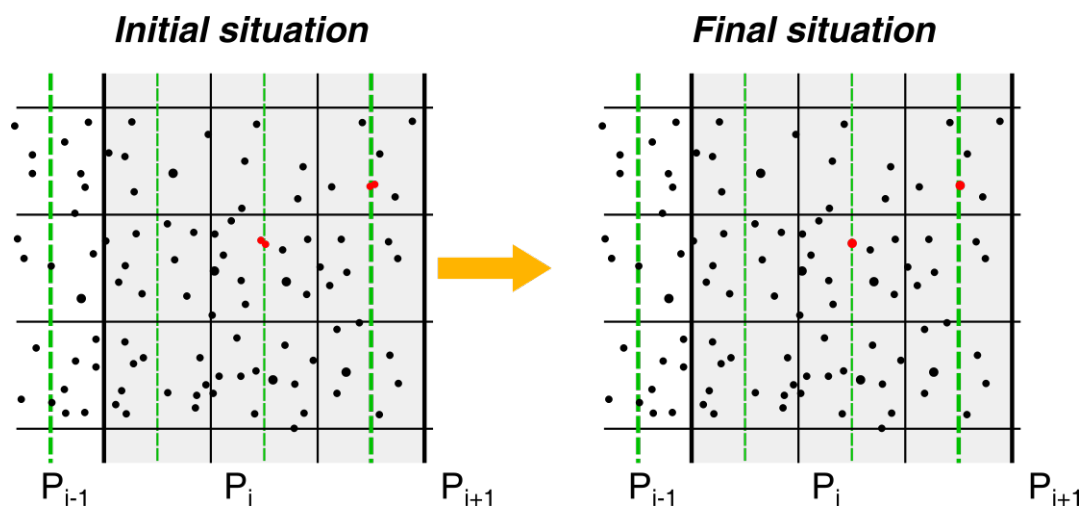


Figure 3.7. Second collision detection. It is carried out on the shifted cells (PHILOFLUID, 2016).

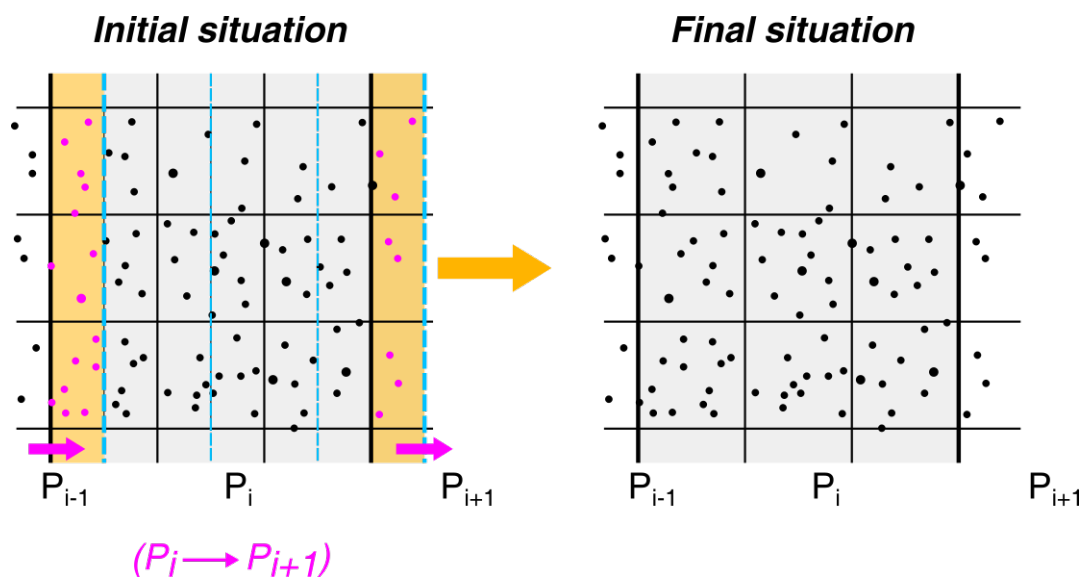


Figure 3.8. The restoring of the original domain decomposition for droplets (PHILOFLUID, 2016).

multiple collisions is allowed in step 3.

# Chapter 4

## Results analysis and conclusion

The computational domain is a parallelepiped and it is obtained by joining two cubes of length  $L$ . In each cube the turbulent velocity field is homogeneous and isotropic, but the global turbulent velocity field in the parallelepiped domain is inhomogeneous along the mixing direction,  $x_3$  in figure 4.1, which is referred to as inhomogeneous direction, while it is still homogeneous in the other two directions,  $x_1$  and  $x_2$  in figure 4.1, which are referred to as homogeneous directions. In order to solve the dissipative scales, an appropriate grid resolution,

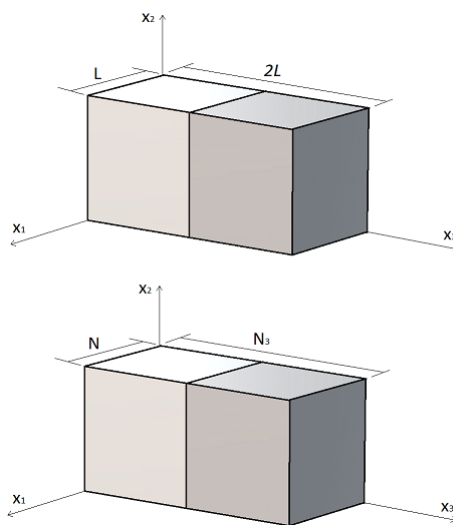


Figure 4.1. The cartoon illustrates in the upper panel the parallelepiped physical domain obtained by the joining two cubes of length  $L$ . In the lower panel the computational domain is shown, where  $N$  and  $N_3$  are the number of grid points along the homogeneous ( $x_1$  and  $x_2$ ) and inhomogeneous ( $x_3$ ) directions respectively.

$\Delta x$ , must be chosen such that the Kolmogorov scale,  $\eta$ , can be solved. The typical value of the Kolmogorov length scale in a warm cloud is of the order of 1 mm. The grid resolution is related to the Kolmogorov scale by the following expression

$$\eta = 2\Delta x$$

where  $\Delta x = 1 \text{ mm}$  in the simulations carried out in this work and consequently the smallest scale solved is  $\eta = 2 \text{ mm}$ . The simulations are carried out using a grid of  $N \times N \times N_3 = 512 \times 512 \times 1024$  points. According to the chosen resolution grid  $\Delta x$ , the physical domain dimensions along the homogeneous and inhomogeneous directions, are

$$L = N\Delta x = 0.512m \quad 2L = 1.024m$$

As already said in Chapter 2 the code works with non-dimensional quantities. The reference length  $L_R$  is defined as the ratio of the homogeneous dimension length  $L$  to  $2\pi$ ,  $L_R = L/2\pi$ . The physical domain non-dimensional lengths, in the homogeneous and inhomogeneous directions respectively, are

$$\tilde{L} = 2\pi \quad 2\tilde{L} = 4\pi$$

The main geometric data are shown in table 4.1. The initial homogeneous and isotropic turbulent velocity field is generated randomly in a cube in accordance with the energy spectrum and the root mean square of the initial velocity imposed by the user (see the initial energy spectrum in figure 4.2). The energy spectrum defines how the energy is distributed on the wavenumbers. In this project only the smallest scales of the inertial range and the scales in the dissipation range are taken into account. The turbulent kinetic energy  $E$  is calculated from the energy spectrum  $E(k)$

$$E = \int_0^\infty E(k)dk$$

The energy dissipation spectrum  $D(k)$  is related to the energy spectrum by the following equation

$$D(k) = 2\nu k^2 E(k) \tag{4.1}$$

where  $k$  is the wavenumber and  $\nu$  is the kinematic viscosity of air. From the equation 4.1, the dissipation rate  $\epsilon$  is obtained

$$\epsilon = \int_0^\infty D(k)dk$$

The turbulent velocity field in the other cube is obtained by multiplying the generated velocity field by a constant value. The constant value is chosen in

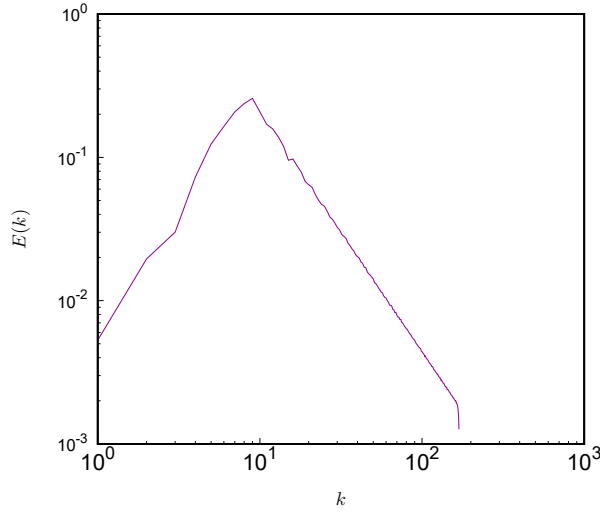


Figure 4.2. The figure shows the initial three dimensional energy spectrum, which is built according to the user’s directives. The energy maximum is at the wavenumber  $k = 8$ .

accordance with the required energy gradient. In this work the initial energy gradient is

$$\frac{E_1}{E_2} = 6.7$$

where the highest energy field ( $E_1$ ) is in the cloud region. The energy spectrum are the same in the two homogeneous and isotropic turbulent fields and so it is the integral length scale. It is important to define the integral scale eddy turnover time,  $\tau$ . The eddy turnover time is the characteristic time associated with that eddy, in particular in our case, the eddy turnover time is associated to the integral scale eddy. In non-dimensional terms the characteristic time  $\tilde{\tau}$  is defined as

$$\tilde{\tau} = \frac{\tilde{l}}{\tilde{u}'}$$

where  $\tilde{l}$  is known from the energy spectrum and  $\tilde{u}' \sim 1$ . The initial velocity field data are shown together with the non-dimensional integral length scale  $\tilde{l}$ , the Taylor microscale  $\tilde{\lambda}$  and the eddy turnover time in the table 4.1. The simulation parameters are shown in table 4.2. The Reynolds number  $Re_{code}$ , that has to be set as a parameter, is calculated with the reference quantities and it is defined as

$$Re_{code} = \frac{U_R L_R}{\nu}$$

<b>Environment data</b>	
$T_0$	281 <i>K</i>
$p_0$	88000 <i>Pa</i>
<b>Geometric and initial data</b>	
$N$	512
$N_3$	1024
$\Delta x$	0.001 <i>m</i>
$L$	0.512 <i>m</i>
$L_R$	0.082 <i>m</i>
$\tilde{l}$	0.39
$\tilde{\lambda}$	$5.39 \times 10^{-2}$
$\tilde{E}$	3.84
$\tilde{\epsilon}$	13.82
$\tilde{\tau}$	0.39

Table 4.1. The table shows the environment temperature and pressure at around 1000 *m* above the sea level. The main geometric data and the data relative to the initial conditions are also shown in this table. The values with the tilde are non-dimensional

<b>Simulations data</b>		
	<b>Saturated case</b>	<b>Supersaturated case</b>
$N_{timestep}$	6500	6500
$\Delta \tilde{t}$	$10^{-4}$	$10^{-4}$
$Re_{code}$	1000	800
$Re_l$	390	312
$Re_\lambda$	53	43
$Sc$	0.61	0.61
$Sc_{mod}$	1.4	1.4
$Pr$	0.71	0.71
$Fr$	0.18	0.18
$N_{drops}$	3840000	3840000
$R_{in}$	2.5 $\mu m$	2.5 $\mu m$

Table 4.2. The table shows the data used for two different simulations carried out in this project, one of them studies a supersaturated cloud region while the other analyse a saturated cloud region.  $N_{drops}$  is the total initial number of water droplets while  $R_{in}$  is their initial radius.

From the  $Re_{code}$ , the Reynolds number relative to the integral length scale  $Re_l$  and the one relative to the Taylor microscale  $Re_\lambda$  can be obtained as follow

$$Re_l = \frac{u'l}{\nu} = Re_{code} \tilde{l} \tilde{u}' \quad Re_\lambda = \frac{u'\lambda}{\nu} = Re_{code} \tilde{\lambda} \tilde{u}'$$

where the tilde symbol  $\sim$  indicates non-dimensional quantities. In order to have a stable simulation, an appropriate time step  $\Delta t$  must be chosen such that a fluid particle moves only a fraction of the grid cell in a time step  $\Delta t$ . An estimate of the Courant number for a typical DNS is given by (Pope, 2000) and the stability condition is approximately

$$\frac{k^{1/2} \Delta t}{\Delta x} = \frac{1}{20}$$

where  $k$  is the turbulent kinetic energy and it is  $k^{1/2} \sim u'$ . The number of eddy turnover time scale,  $n_\tau$ , that has been simulated can be computed from the values of the total number of time steps  $N_{timestep}$  and the time step  $\Delta \tilde{t}$

$$n_\tau = \frac{N_{timestep} \Delta \tilde{t}}{\tilde{\tau}} = \frac{6500 \cdot 10^{-4}}{0.39} \sim 1.7$$

where the  $\tilde{\tau}$  is the non-dimensional eddy turnover time (see table 4.1). Almost two time scales are simulated. The Froude number is very low, this indicates that the flow simulated is strongly stratified. An initial monodisperse homogeneous distribution of water particles is taken into account. The droplets are initially distributed only in the cloud region and their initial radius is  $R_{in} = 2.5 \mu m$ . The domain volume in the cloud region is  $V_{cloud} = 51.2^3$ , so the water particles number density is  $n_{drop} \sim 29 \text{ 1/cm}^3$ . Two different simulations was carried out in this project. They differ in the Reynolds number (see table 4.2) and in the initial water vapour density profile (see figure 4.3). In the first simulation the cloud region is supersaturated (see the vapour density profile in figure 4.3 (a)), while in the second simulation the cloud region is just saturated (see vapour density profile in figure 4.3 (b)) Both simulations studies an unstable stratification according to the initial temperature perturbation of the atmospheric standard temperature gradient. The figure 4.4 shows the temperature perturbation at the cloud-clear air interface. The cloud region is warmer than the upper region (environmental air). This is a reason for instability, due to the buoyancy effect. As already mentioned in the Chapter 2, in this work a the time decaying turbulent shearless mixing layer is simulated. The production of turbulent kinetic energy is not taken into account and only the gradient of energy between the two HIT (homogeneous and isotropic turbulence) fields is considered, while the integral length scale is the same in the whole domain.

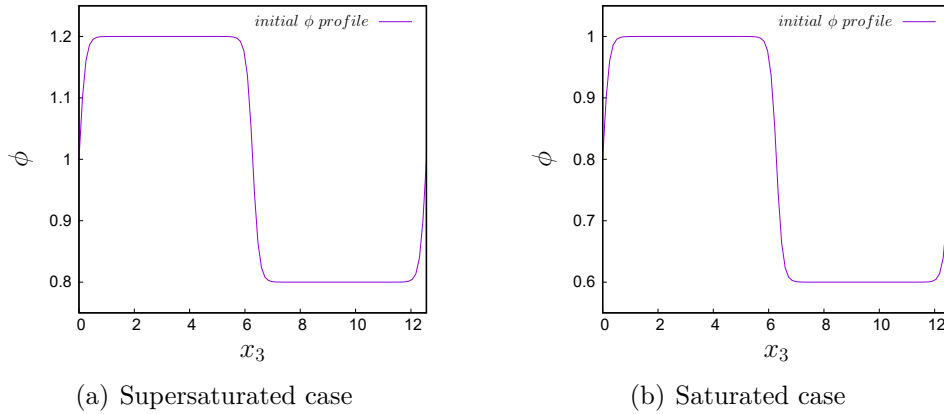


Figure 4.3. The figure shows the initial water vapour density profiles for the supersaturated (a) and the saturated (b) cases. In the figures  $\phi$  is defined as the ratio of the vapour density at the temperature  $T$  to the saturated vapour density at the same temperature  $\phi = \rho_v(T)/\rho_{vs}(T)$ .

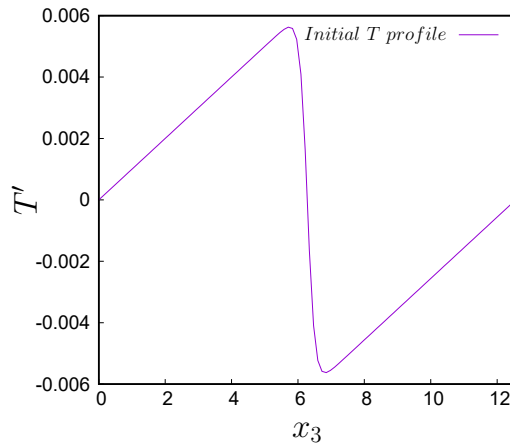


Figure 4.4. The initial temperature profile. The temperature variation,  $\Delta T$ , at the cloud-clear air interface is  $(T - T_0)/T_0 \sim -0.012$ .

The results for the turbulent velocity field, which are shown below, are referred to the saturated case, the case with the highest Reynolds number, but the statistic trend is the same of the lower Reynolds case. In figure 4.5 the time decay of the mean value of the energy associated with the component of velocity  $u_3$ , in the  $x_3$  inhomogeneous direction. The figure was obtained by averaging the energy on each plane normal to the inhomogeneous direction and then by plotting  $\overline{u_3^2}(x_3)$ . Other informations about the turbulent mixing

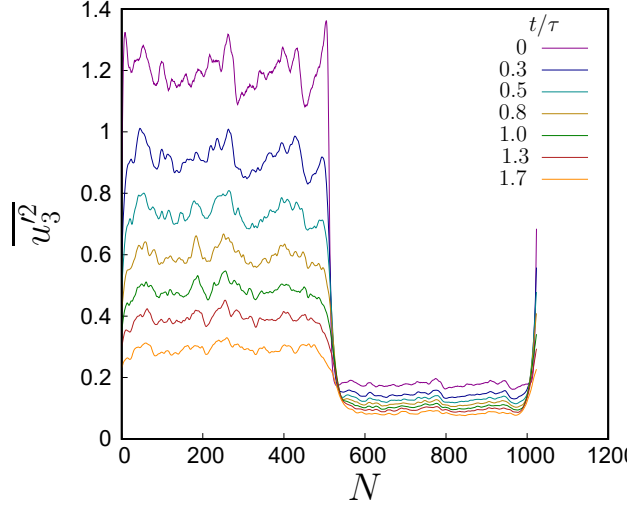


Figure 4.5. The figure shows the time decay of the energy associated with the velocity component in the inhomogeneous direction,  $\overline{u'^2}$ . The time range is from  $t/\tau = 0$  to  $t/\tau = 1.7$ . This results has been obtained for  $Re_\lambda = 53$ .

layer simulated can be obtained by the statistics analysis of the velocity field. In particular the focus is on the analysis of the normalized third (skewness) and fourth (kurtosis) single-point moments of the velocity components and of the longitudinal velocity derivative. The skewness and kurtosis for example of a velocity component  $u$ , are defined as

$$S_u = \frac{\overline{u'^3}}{\overline{u'^2}^{3/2}}$$

$$K_u = \frac{\overline{u'^4}}{\overline{u'^2}^2}$$

where the overline indicates the spatial average on the planes at constant  $x_3$  (direction normal to the mixing layer). In figure 4.6 (a) the skewness of the velocity component  $u_3$  is shown, while in figure 4.6 (b) the kurtosis of the same velocity component is shown. Outside the mixing layer the skewness value oscillates around the zero while the kurtosis around the value 3. Since  $S = 0$  and  $K = 3$  are the values of the Gaussian distribution which describes the homogeneous and isotropic turbulent field, the small oscillation around  $S = 0$  and  $K = 3$  confirms the fact that the two turbulent field are initially homogeneous and isotropic. In the mixing region the skewness reach a maximum (at  $t/\tau = 0.77$ ) which gradually decreases with time and moves towards the low variance region, due to the initial energy gradient. The kurtosis shares the

same trend of the skewness. The flow is largely intermittent and the positions along  $x_3$  of the skewness,  $x_s$ , and kurtosis,  $x_k$ , maxima, moving towards the low energy region, represent the penetration of the turbulent mixing. At  $x_s$  the turbulent kinetic energy flow is maximized and it occurs on a plane moving gradually towards the low energy region. The longitudinal velocity skewness

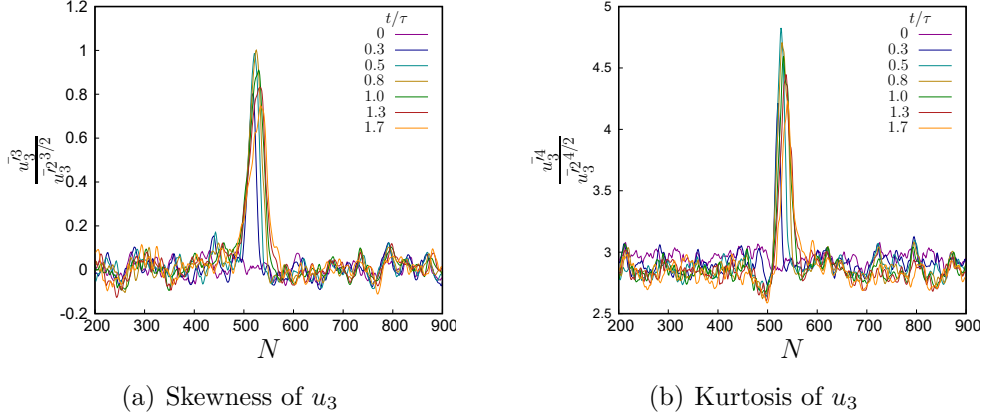


Figure 4.6. The figure shows the time evolution of the normalized third and fourth order moments of the velocity component  $u_3$ . Data obtained for Taylor microscale Reynolds number  $Re_\lambda = 53$  and a time range from  $t/\tau = 0$  to  $t/\tau = 1.7$ .

and kurtosis in the inhomogeneous direction (normal to the mixing layer) is shown in figure 4.7 while the longitudinal velocity skewness and kurtosis in the homogeneous direction (parallel to the mixing layer) is shown in figure 4.8. The longitudinal skewness in direction normal to the mixing layer (figure 4.7 (a)) shows a negative peak at the mixing layer. The opposite trend but less intense is shown by the longitudinal derivative skewness in direction parallel to the mixing (figure 4.8 (b)) where the peak is positive respect to the isotropic value. In both cases the skewness maxima gradually move with time towards the low energy region. In the same positions of skewness maxima, both the longitudinal velocity derivative kurtosis normal to the mixing layer (figure 4.7 (b)) and the one parallel to the mixing layer (figure 4.8 (b)) show a positive peak. Physically the departure of skewness from the isotropic values reduces the compression on fluid filaments in the directions parallel to the mixing layer while the filaments compression normal to the layer is enhanced respect to the isotropy (Tordella & Iovieno, 2011). The time evolution visualization of the turbulent kinetic energy flow field is shown, for the supersaturated case in figure 4.9 where the development of the mixing layer between two homogeneous and isotropic turbulent fields is shown. The passive scalar turbulent trans-

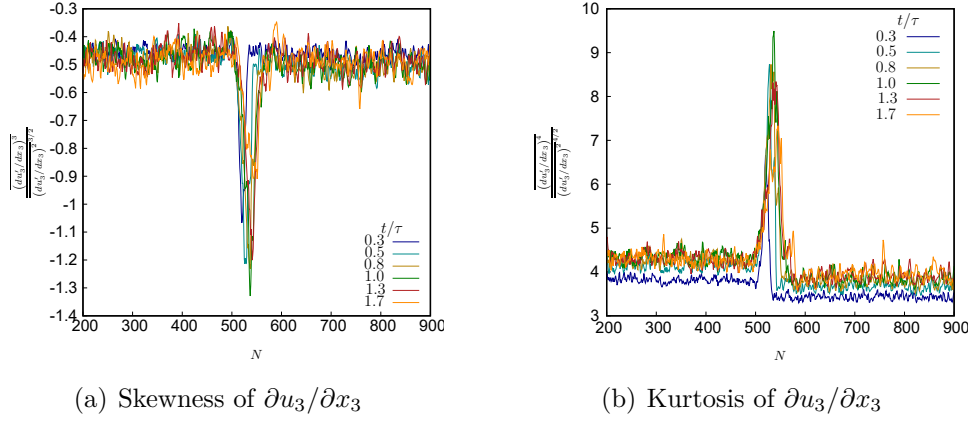


Figure 4.7. The figures show the time evolution of the skewness (a) and kurtosis (b) of the longitudinal velocity derivative in direction normal to the mixing layer,  $\partial u_3/\partial x_3$ . Data obtained for Taylor microscale Reynolds number  $Re_\lambda = 53$  and a time range from  $t/\tau = 0$  to  $t/\tau = 1.7$

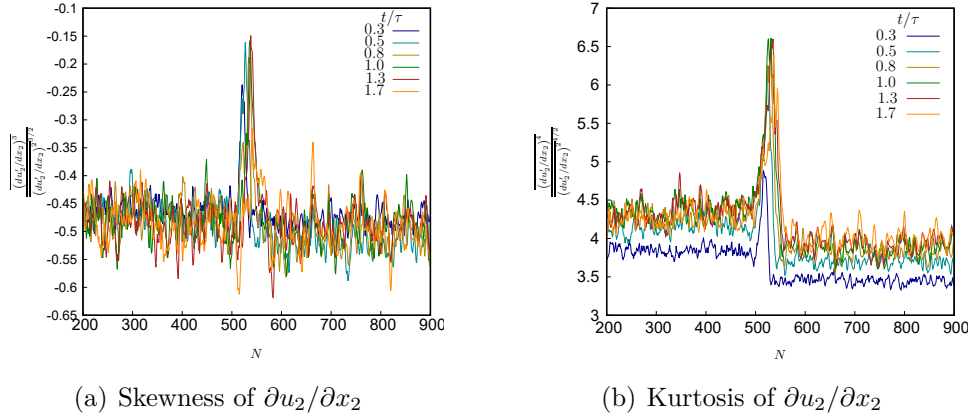


Figure 4.8. The figures show the time evolution of the skewness (a) and kurtosis (b) of the longitudinal velocity derivative in direction parallel to the mixing layer,  $\partial u_2/\partial x_2$ . Data obtained for Taylor microscale Reynolds number  $Re_\lambda = 53$  and a time range from  $t/\tau = 0$  to  $t/\tau = 1.7$ .

port across the interface is also described. Two passive scalars are taken into account: the temperature,  $T$ , and the ratio of the water vapour density to the saturated vapour density at the same temperature,  $\phi$ . The time evolution of the mean values of the temperature and of the vapour density are shown for the supersaturated case in figure 4.10 and for the saturated case in figure

4.11. A slight widening of the mixing layer thickness can be observed as the flow evolves in time. The increase of the layer thickness cannot be appreciate much due to the short time range simulated which is less than two eddy turnover time. The variance of the passive scalar  $\theta$  is defined as  $\overline{\theta'^2}$  where  $\theta' = \theta - \bar{\theta}$  is the scalar fluctuation. The variance of the temperature field and of the vapour density, obtained by averaging the square of their respective fluctuation on each plane parallel to the interface, is shown in figure 4.13 for the saturated case. The variance shows a high peak centred on the scalar interface. The variance results for the supersaturated case show the same trend of the saturated case (see figure 4.12). While the variance time evolution is not affected by the energy gradient between the two turbulent regions, its influence is evident in the higher order moments such that the skewness and the kurtosis of the passive scalars. The figure 4.14 (a) shows, for the high Reynolds number case (saturated case), the skewness of the temperature while the temperature kurtosis is shown in figure 4.14 (b). These figures show two peaks at the edges of the mixing layer. Between the two peaks both skewness and kurtosis values are close to the Gaussian ones. This means that the passive scalar skewness and kurtosis evolution are characterized by two largely intermittent fronts. The presence of two intermittent fronts is related to the deformation of the initial plane interface, in particular they are located where high scalar gradients are located. These results agree with those obtained by Iovieno *et al.* (2014). The asymmetry in the skewness and kurtosis maxima locations is due to turbulent kinetic energy gradient. The same statistical trend is shown in figure 4.15, which illustrates the skewness and kurtosis of the water vapour density for the same simulation. From the comparison of the results obtained for the saturated case simulation (see figures 4.15 and 4.14) with the results obtained for the supersaturated case simulation (see figures 4.17 and 4.16), it can be seen that the two peaks relative to the two fronts, are smaller leading to the conclusion that the Reynolds number affects the intensity of the intermittency level, in particular the higher the Reynolds the larger is the intermittency as shown by (Iovieno *et al.*, 2014). An other difference is in the extreme asymmetry in the skewness and kurtosis profiles of the temperature and water vapour density for the supersaturated case simulation. The water vapour density skewness and kurtosis (see figures 4.17 (a) and (b)) show that the vapour fluctuations in the cloud region are really large. Maybe this very high fluctuations intensity is due to the water droplets feedback on the vapour density field. The same conclusions can be made for the normalized third and fourth order moments of the temperature, which is affected by the condensation latent heat release. In the figures 4.18 and 4.19 the visualizations of the temperature and the water vapour density fields at three different instants are

shown respectively. In these figures the time evolution of the interface can be seen together with the entrainment of the clear air into the cloud region.

## 4.1 Water droplets dynamics analysis

The two simulations carried out in this work describe two opposite situations. In the first simulation the cloud region is saturated,  $\phi = 1$ , and the clear air region is subsaturated,  $\phi = 0.6$ , while in the second simulation the cloud region is supersaturated,  $\phi = 1.2$ , and the clear air is subsaturated,  $\phi = 0.8$ , but with a higher water vapour density than it is in the other simulation. The results obtained from the two simulations are shown in this section, in particular the time evolution of the droplet size distribution and the clustering (or preferential concentration) phenomenon are described. In figure 4.20 the water droplets number distribution in the inhomogeneous direction  $x_3$  is shown. At the initial condition the particles concentration is homogeneous, but after around  $0.77 \tau$  large fluctuations in the number of water droplets can be seen. The strongly oscillating droplet number profile does not vary with time after around one eddy turnover time, giving some rough information about the clustering phenomenon. While in the supersaturated case (see figure 4.20 (a)) some particles moves towards the clear air region, in the saturated case (figure 4.20 (b)) not only the particles does not move to the subsaturated region but many of them evaporate completely. The complete evaporation of particles is evident from the narrowing of the droplets number profile, where the narrowing is related to the entrainment of the clear and subsaturated air at the interface. In order to have also some information on the liquid water content distribution in the inhomogeneous direction, the liquid water total volume was computed in each plane parallel to the mixing layer. The results are shown in figure 4.21, where the liquid water total volume is calculated by summing the volume of all the droplets that are in the plane at constant  $x_3$  and using the non-dimensional normalized water particles radius. In the supersaturated case the total volume in each plane increases with time due to the condensation of water vapour, while the opposite trend can be seen in the saturated case where the total volume in each plane reduces with time until it reaches almost the zero value at  $t/\tau = 1.7$ , due to the intense evaporation experienced by the droplets when subsaturated air is entrained. The strong reduction of water droplets radius with time and the intense evaporation that occurs in the saturated case simulation are shown in figure 4.22 where the droplets spatial distribution is illustrated at  $t/\tau = 0$ ,  $t/\tau = 0.8$  and  $t/\tau = 1.7$ . In figure 4.22 the particles colour indicates the non-dimensional and normalized particle radius,  $R/R_{in}$ . Near the interface the particles radius is much smaller

than the radius of droplets in the centre of the cloud region, far from the interface. Furthermore it can be seen the reduction of the number of particles near the interface due to their complete evaporation, caused by the strong dilution due to the entrainment of subsaturated clear air into the cloud region at the interface. The time evolution of the water droplets size distribution for both the saturated and supersaturated cases is shown in figure 4.23. A slight broadening of the water droplet size distribution with time can be seen in both cases, but while in the supersaturated case (see figure 4.24 (a)) the mean droplet radius increase from  $R/R_{in} = 1$  to around  $R/R_{in} = 1.4$ , in the saturated case (see figure 4.24 (b)) it decrease from  $R/R_{in} = 1$  to around  $R/R_{in} = 0.2$ . Since the figure 4.23 shows a global view of the time evolution of the water droplets size distribution, but it does not show the shapes of the size distributions, single water particles radii distributions are shown for the supersaturated case in figure 4.25 and for the saturated case in figure 4.26. As already mentioned in Chapter 2 and 3 the water droplets are advected by the small scales of turbulence. The turbulent transport of the inertial particles leads to a spatial preferential concentration of the droplets. In particular water particles move towards region where the vorticity intensity is low. The clustering phenomenon is a fundamental process in the warm rain formation since it enhances the turbulent collisions between particles. It depends on the droplets inertial response time to the turbulent velocity field changes. In figures 4.27, 4.28 and 4.29 the water droplets spatial distributions, for the supersaturate case, are shown together with the concentration of droplets in three different slices at  $x_3 = 3$ ,  $x_3 = 4$  and  $x_3 = 5$ , for the time instants  $t/\tau = 0$ ,  $t/\tau = 0.8$  and  $t/\tau = 1.7$  respectively. As said before the water particles, due to their inertia, are subject to the centrifugal forces and for this reason they are pushed out from the region at high vorticity towards regions where the vorticity intensity is lower. In figure 4.30 the overlapping of the water droplets spatial distribution on the enstrophy flow visualization is shown at three time instants  $t/\tau = 0$  (a),  $t/\tau = 0.8$  (b) and  $t/\tau = 1.7$  (c). The enstrophy is defined as the square of the vorticity  $\omega^2$  and it gives informations on the vorticity intensity level. The visualization in figure 4.30 confirms the facts that the inertial particles concentrates in the low vorticity regions and it agrees with the figure 3.3 in Chapter 3. The same visualization but for the saturated case is shown in figure 4.31.

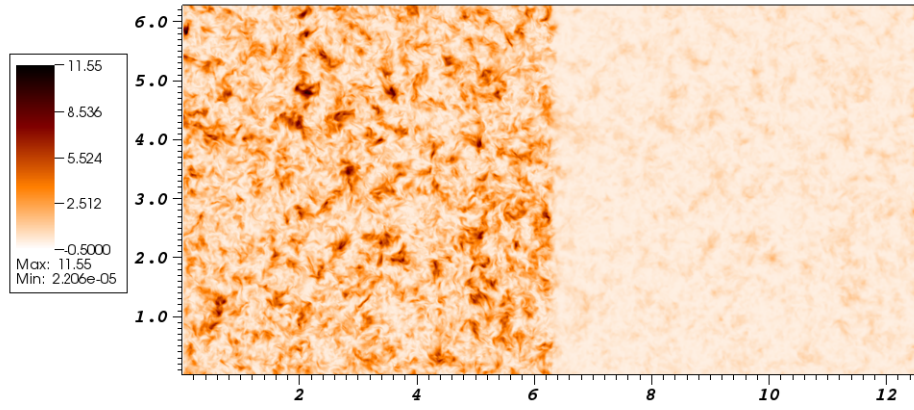
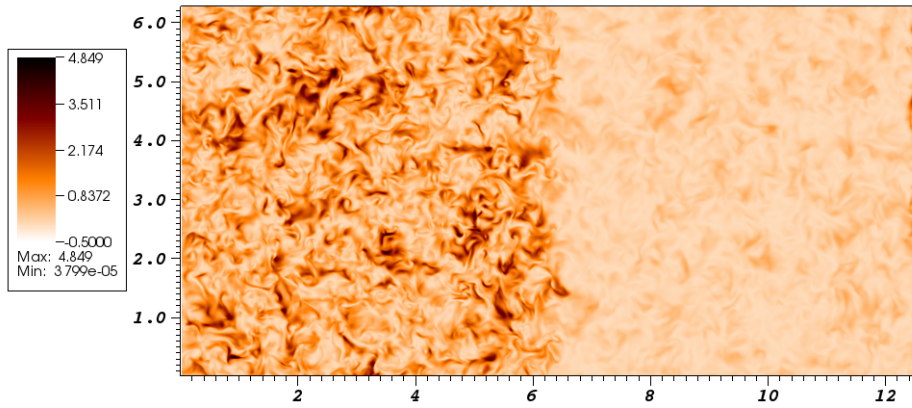
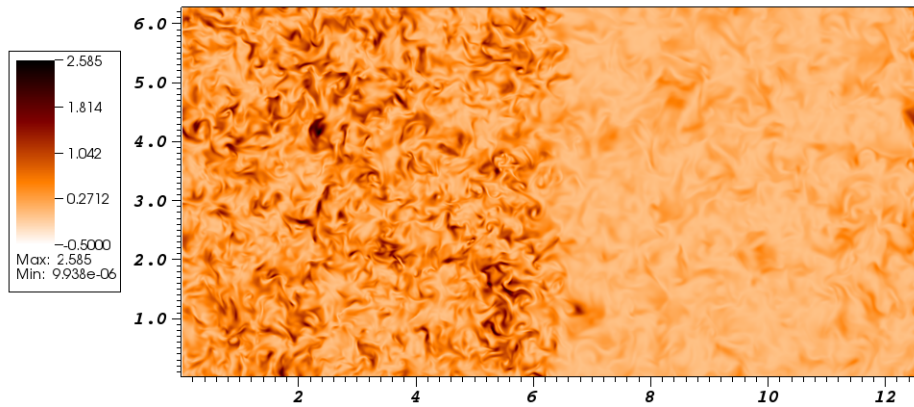
(a)  $t/\tau = 0$ (b)  $t/\tau = 0.8$ (c)  $t/\tau = 1.7$ 

Figure 4.9. In the figure the energy field is shown at three time instants,  $t/\tau = 0$  (a),  $t/\tau = 0.8$  (b) and  $t/\tau = 1.7$  (c). Visualization obtained for a Taylor microscale Reynolds number  $Re_\lambda = 43$

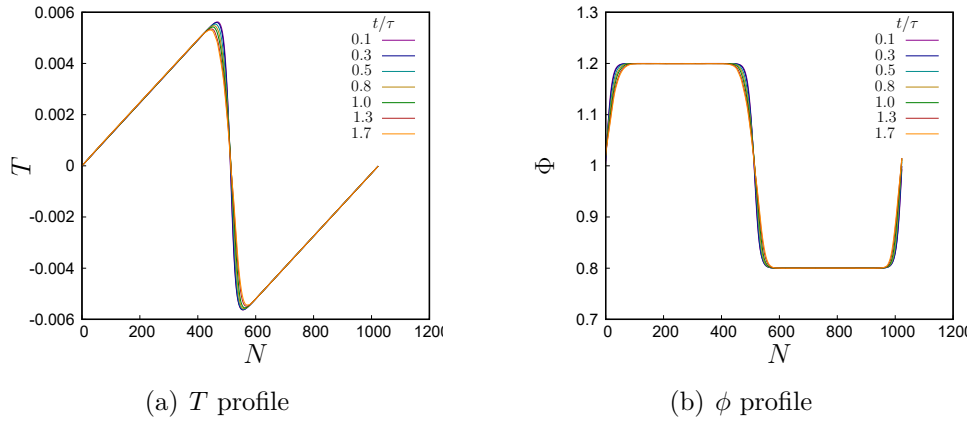


Figure 4.10. The figures show the time evolution of the mean values of temperature,  $T$ , (a) and of the ratio of water vapour density to saturated vapour density,  $\phi$ , (b) profiles for the simulation that studies a supersaturated cloud region. Data obtained for Taylor microscale Reynolds number  $Re_\lambda = 43$  and a time range from  $t/\tau = 0.13$  to  $t/\tau = 1.7$ .

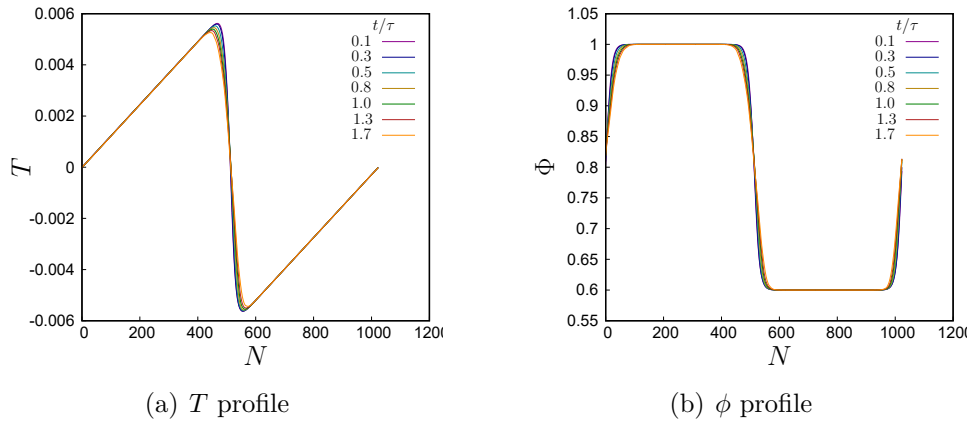


Figure 4.11. The figures show the time evolution of the mean values of temperature,  $T$ , (a) and of the ratio of water vapour density to saturated vapour density,  $\phi$ , (b) profiles for the simulation that studies a just saturated cloud region. Data obtained for Taylor microscale Reynolds number  $Re_\lambda = 53$  and a time range from  $t/\tau = 0.13$  to  $t/\tau = 1.7$ .

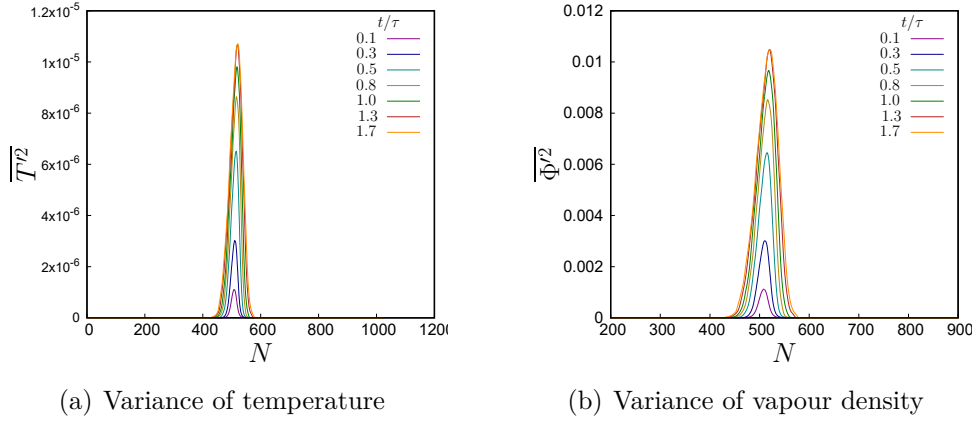


Figure 4.12. The figures show the time evolution of the variance of temperature,  $\overline{T'^2}$ , (a) and of the ratio of water vapour density to saturated vapour density,  $\overline{\phi'^2}$ , (b) profiles for the supersaturated case. Data obtained for Taylor microscale Reynolds number  $Re_\lambda = 43$  and a time range from  $t/\tau = 0.13$  to  $t/\tau = 1.7$ .

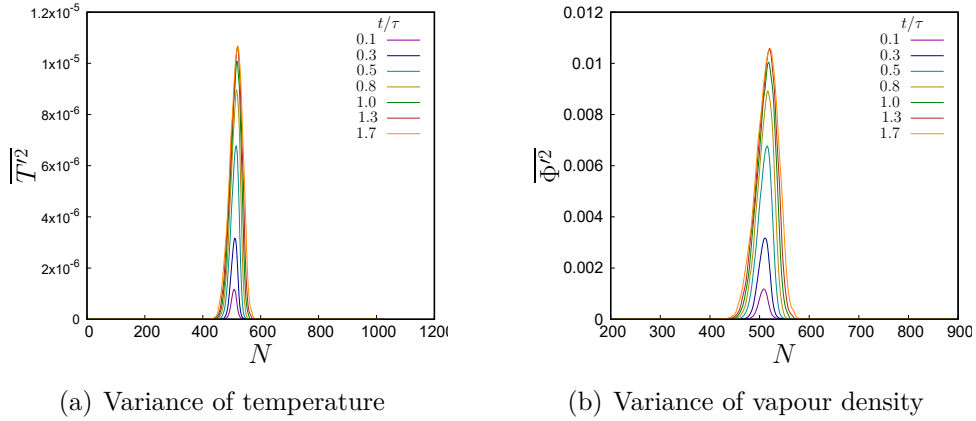


Figure 4.13. The figures show the time evolution of the variance of temperature,  $\overline{T'^2}$ , (a) and of the ratio of water vapour density to saturated vapour density,  $\overline{\phi'^2}$ , (b) profiles for the saturated case. Data obtained for Taylor microscale Reynolds number  $Re_\lambda = 53$  and a time range from  $t/\tau = 0.13$  to  $t/\tau = 1.7$ .

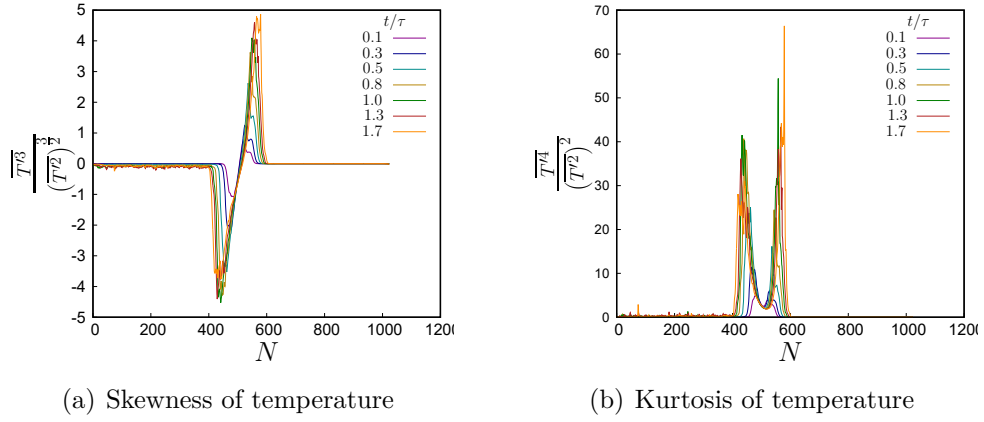


Figure 4.14. The figures show the time evolution temperature skewness (a) and kurtosis (b). Data obtained for Taylor microscale Reynolds number  $Re_\lambda = 53$  and a time range from  $t/\tau = 0.13$  to  $t/\tau = 1.7$ .

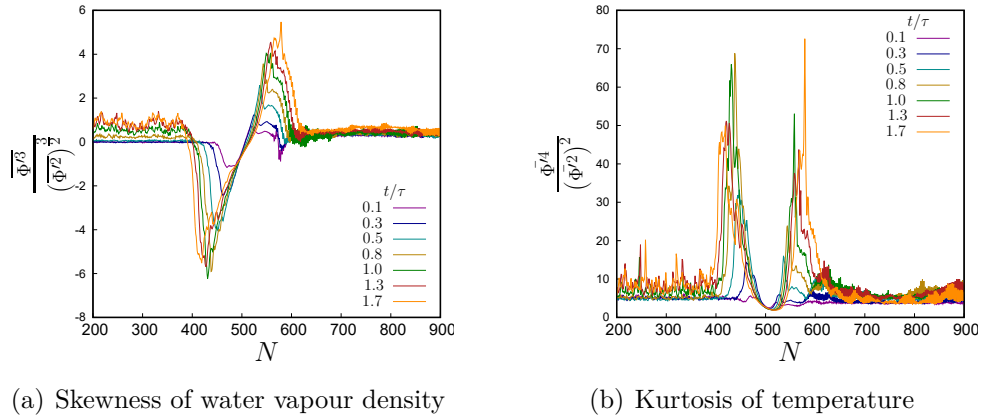


Figure 4.15. The figures show the skewness (a) and kurtosis (b) of the ratio of the water vapour density to the saturated vapour density. Data obtained for Taylor microscale Reynolds number  $Re_\lambda = 53$  and a time range from  $t/\tau = 0.13$  to  $t/\tau = 1.7$ .

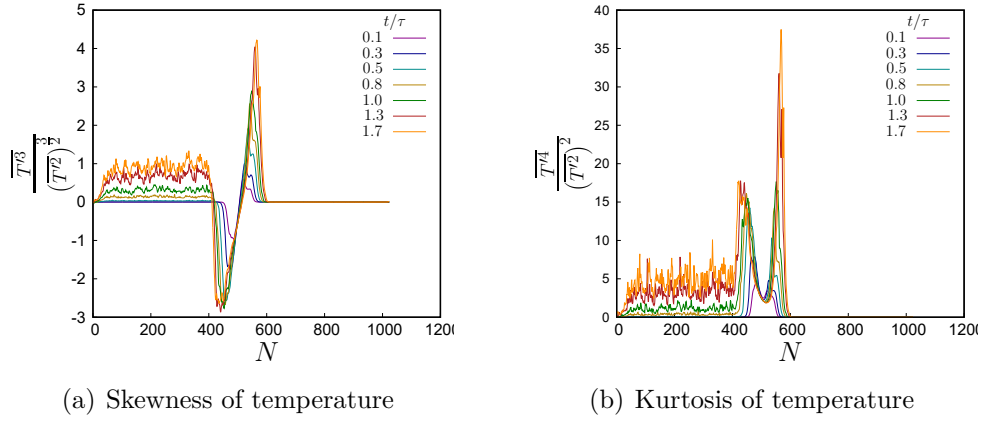


Figure 4.16. The figures show the time evolution temperature skewness (a) and kurtosis (b). Data obtained for Taylor microscale Reynolds number  $Re_\lambda = 43$  and a time range from  $t/\tau = 0.13$  to  $t/\tau = 1.7$ .

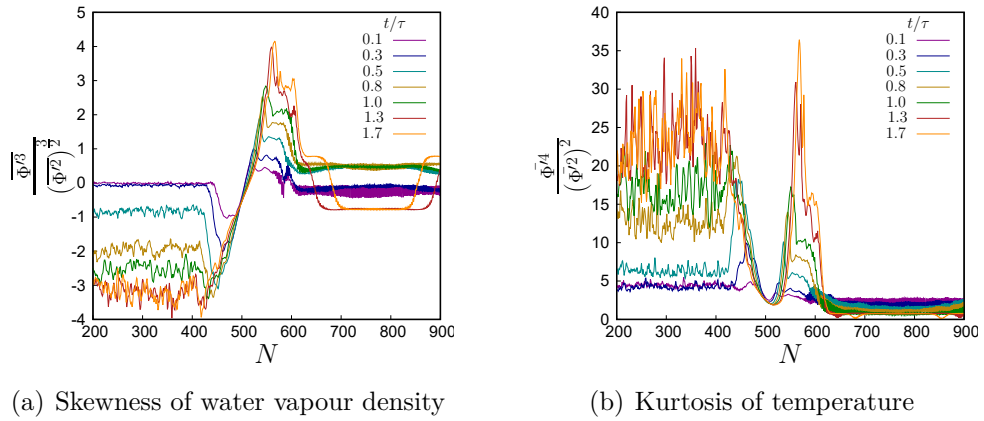


Figure 4.17. The figures show the skewness (a) and kurtosis (b) of the ratio of the water vapour density to the saturated vapour density. Data obtained for Taylor microscale Reynolds number  $Re_\lambda = 43$  and a time range from  $t/\tau = 0.13$  to  $t/\tau = 1.7$ .

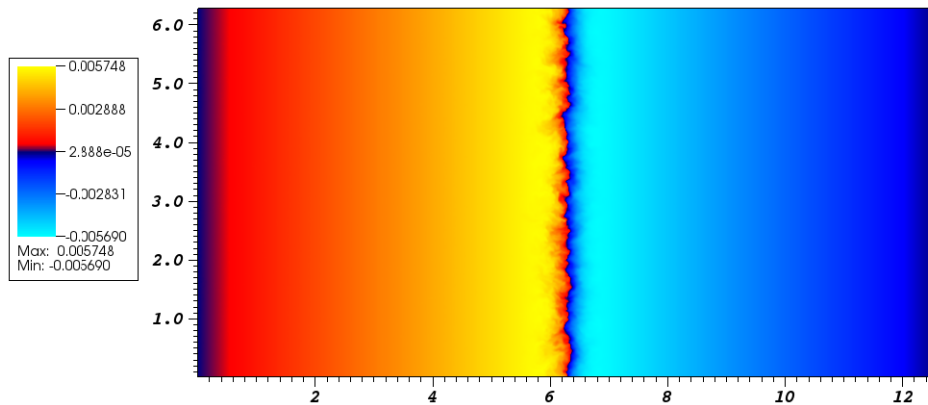
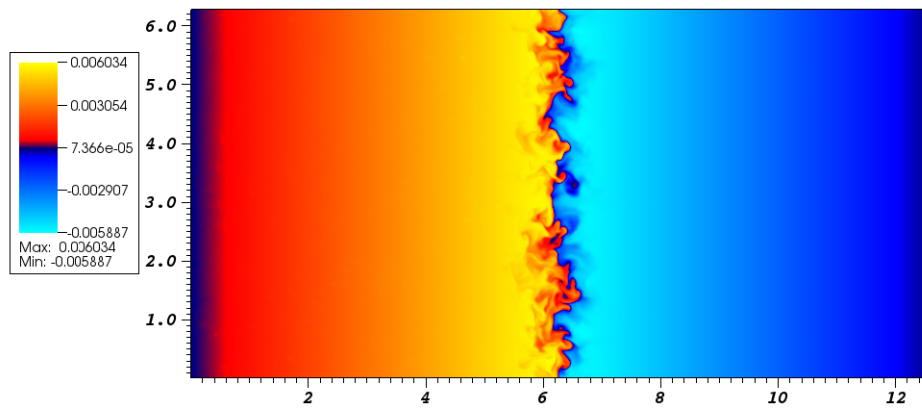
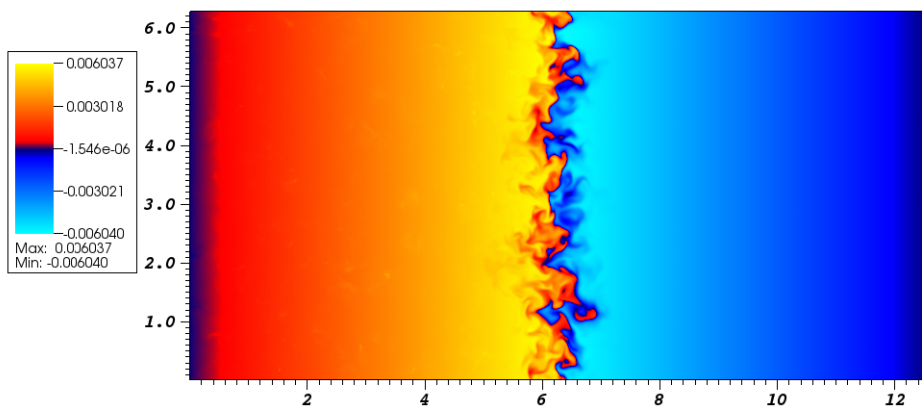
(a)  $t/\tau = 0$ (b)  $t/\tau = 0.8$ (c)  $t/\tau = 1.7$ 

Figure 4.18. In the figure the temperature field is shown at three time instants,  $t/\tau = 0$  (a),  $t/\tau = 0.8$  (b) and  $t/\tau = 1.7$  (c). Visualization obtained for a Taylor microscale Reynolds number  $Re_\lambda = 43$

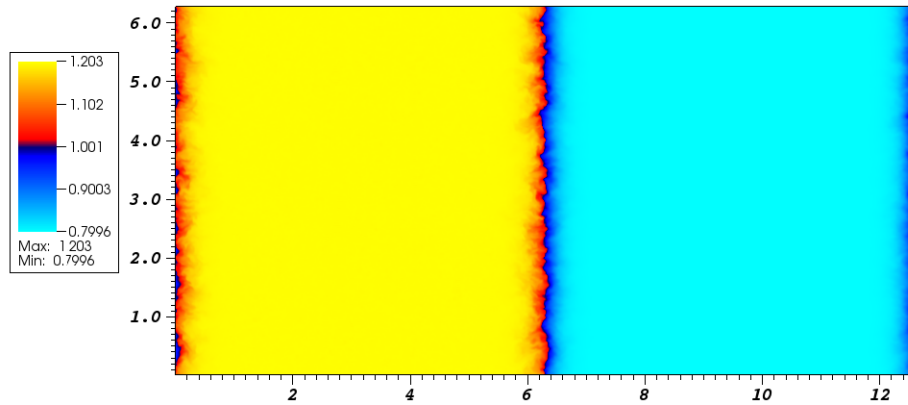
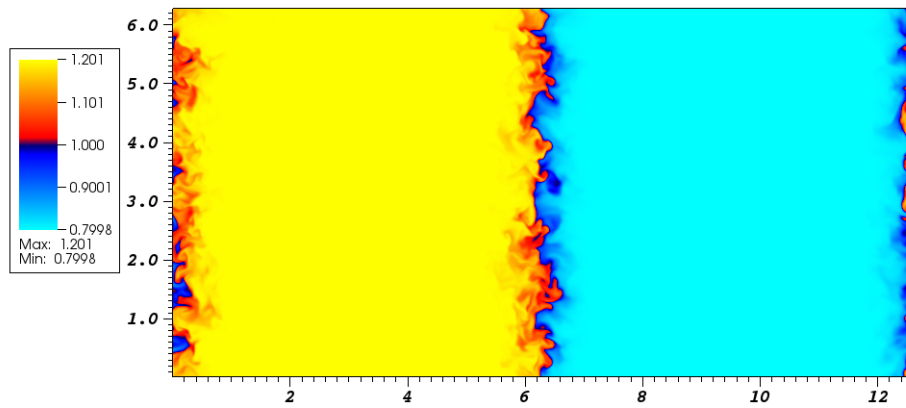
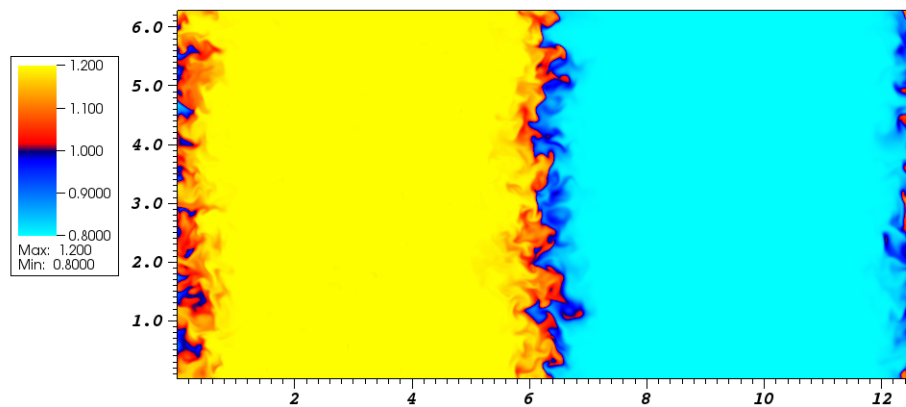
(a)  $t/\tau = 0$ (b)  $t/\tau = 0.8$ (c)  $t/\tau = 1.7$ 

Figure 4.19. In the figure the water vapour density field is shown at three time instants,  $t/\tau = 0$  (a),  $t/\tau = 0.8$  (b) and  $t/\tau = 1.7$  (c). Visualization obtained for a Taylor microscale Reynolds number  $Re_\lambda = 43$

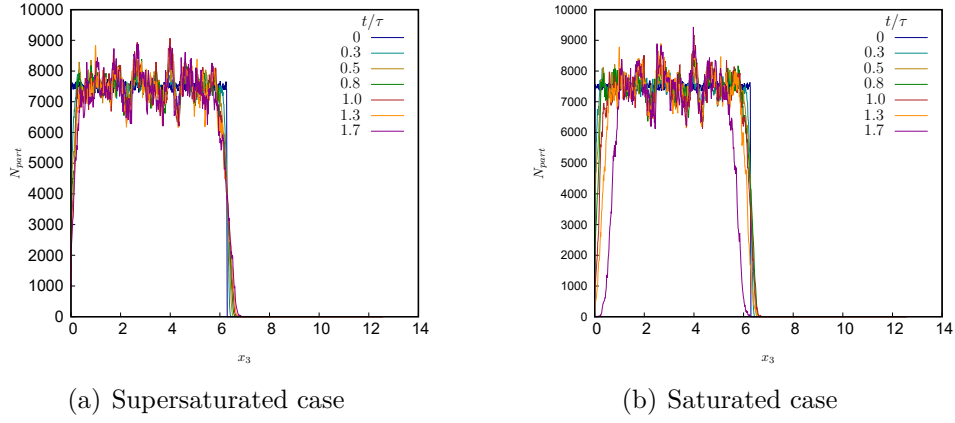


Figure 4.20. The figures show the distribution of the number of the water droplets in the inhomogeneous direction  $x_3$  for the supersaturated case (a) and for the saturated case (b). The time range is from  $t/\tau = 0$  to  $t/\tau = 1.7$ .

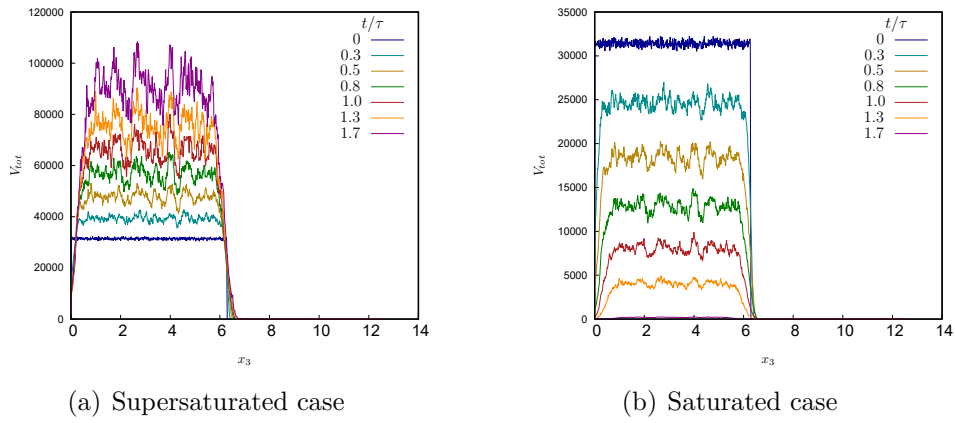


Figure 4.21. The figures show the distribution of the water droplets total volume in the inhomogeneous direction  $x_3$  for the supersaturated case (a) and for the saturated case (b). The time range is from  $t/\tau = 0$  to  $t/\tau = 1.7$ .

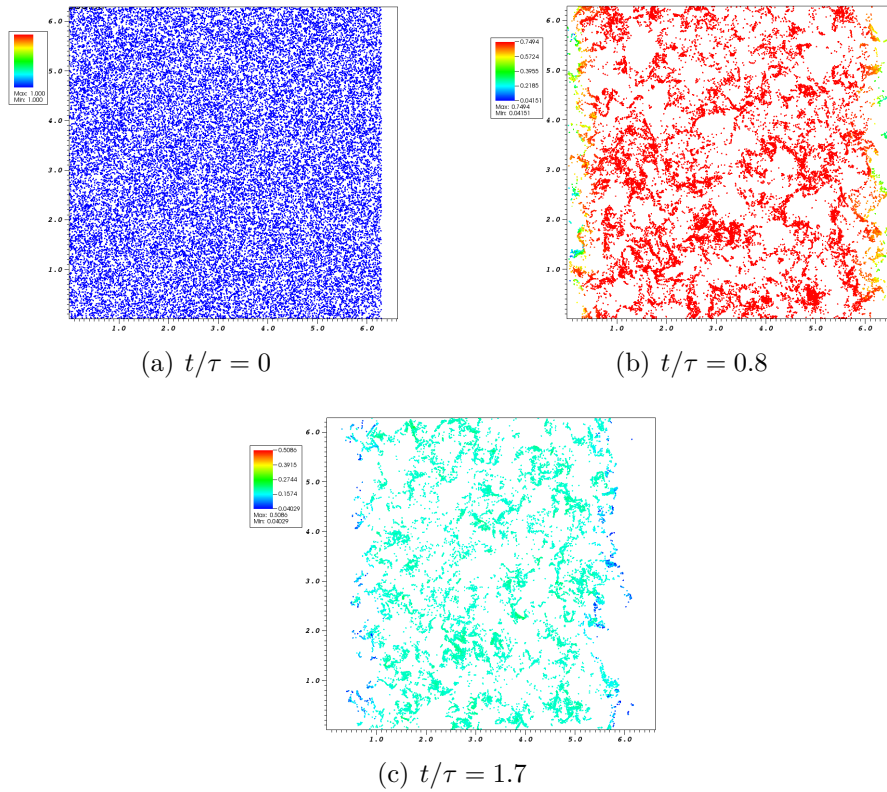
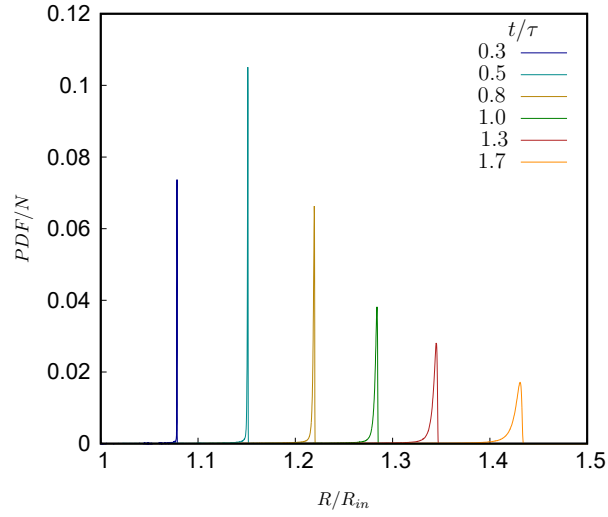
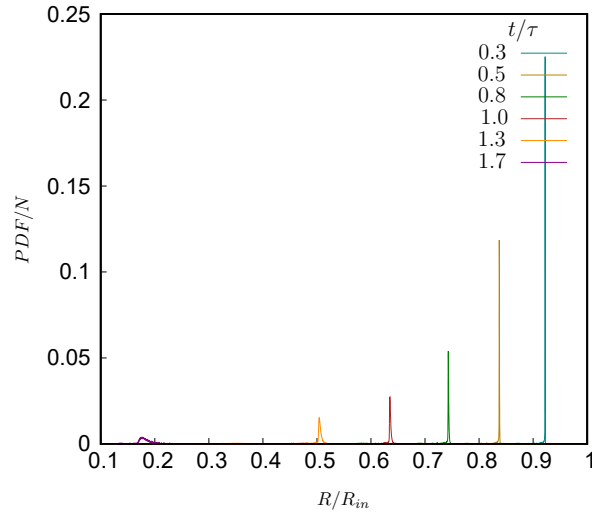


Figure 4.22. The figures show the water droplets spatial distribution at  $t/\tau = 0$ ,  $t/\tau = 0.8$  and  $t/\tau = 1.7$ , for the saturated case. The dots show the particles positions while the dots colour gives information on the particles radius. The initial non-dimensional and normalized radius is  $R/R_{in} = 1$ .



(a) Supersaturated case



(b) Saturated case

Figure 4.23. The figures show the water droplets size distribution for the supersaturated case (a) and for the saturated case (b). The initial non-dimensional normalized radius is  $R/R_{in} = 1$ . The time range is from  $t/\tau = 0.26$  to  $t/\tau = 1.7$ .

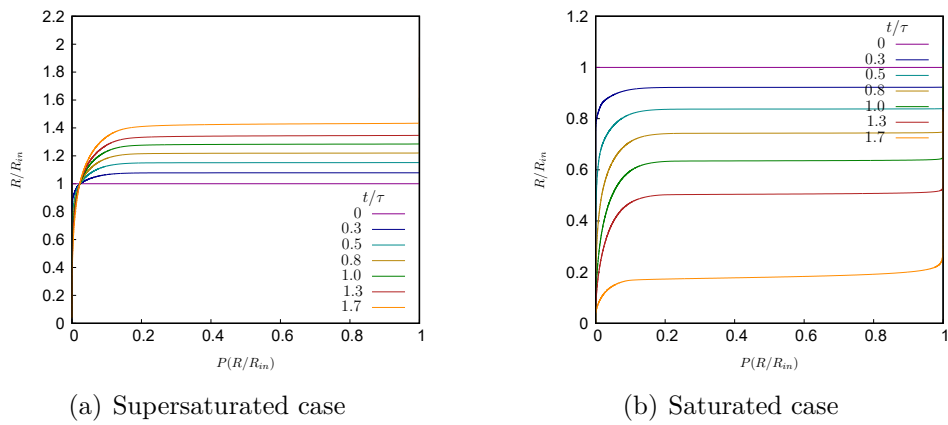


Figure 4.24. The figures show the distribution function (cumulant) for the supersaturated case (a) and for the saturated case (b). The initial non-dimensional normalized radius is  $R/R_{in} = 1$ . The time range is from  $t/\tau = 0$  to  $t/\tau = 1.7$ .

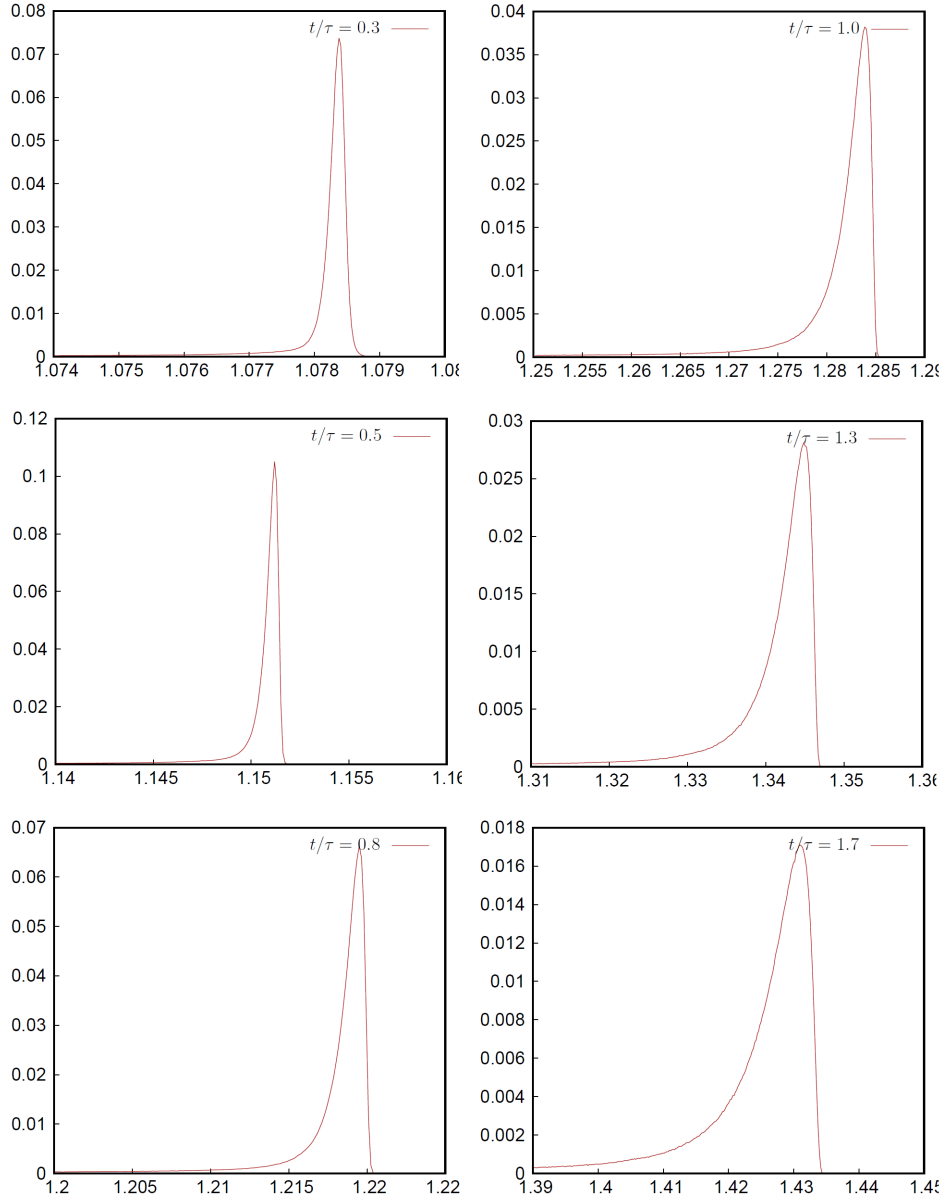


Figure 4.25. The water droplets size distributions are illustrated for the supersaturated case. The single size distributions are shown at different instants of time, from the top left downwards and then from the top right downwards  $t/\tau = 0.3$ ,  $t/\tau = 0.5$ ,  $t/\tau = 0.8$ ,  $t/\tau = 1$ ,  $t/\tau = 1.3$ ,  $t/\tau = 1.7$ . The initial non-dimensional normalized radius is  $R/R_{in} = 1$ , the Taylor microscale Reynolds number is  $Re_\lambda = 43$  and the initial water droplets concentration is  $n_{drops} = 29 \text{ 1/cm}^3$ .

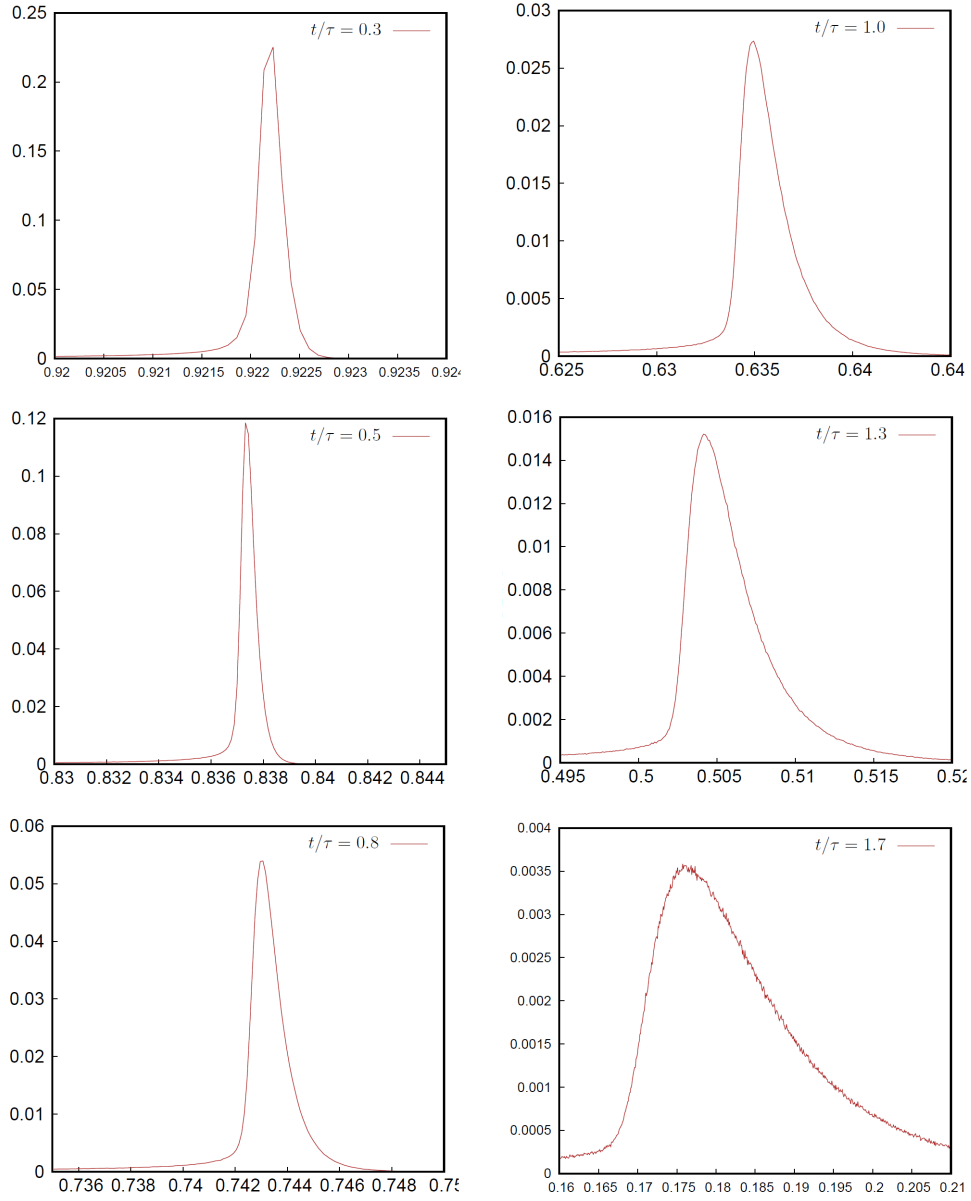
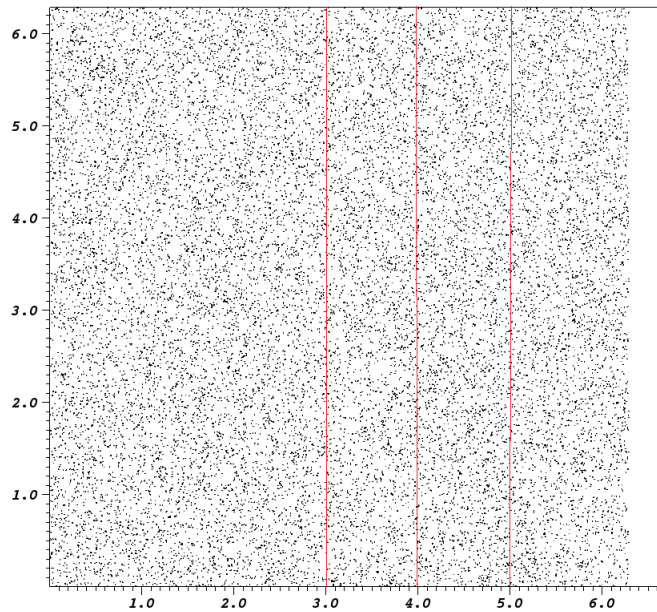
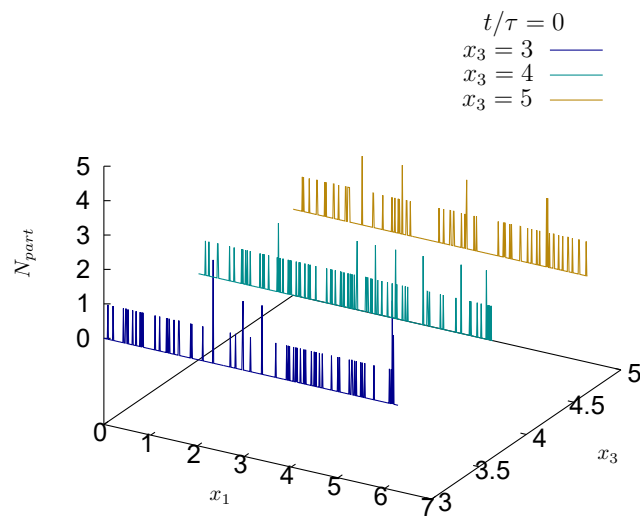


Figure 4.26. The water droplets size distributions are illustrated for the saturated case. The single size distributions are shown at different instants of time, from the top left downwards and then from the top right downwards  $t/\tau = 0.3$ ,  $t/\tau = 0.5$ ,  $t/\tau = 0.8$ ,  $t/\tau = 1$ ,  $t/\tau = 1.3$ ,  $t/\tau = 1.7$ . The initial non-dimensional normalized radius is  $R/R_{in} = 1$ , the Taylor microscale Reynolds number is  $Re_\lambda = 53$  and the initial water droplets concentration is  $n_{drops} = 29 \text{ 1/cm}^3$ .

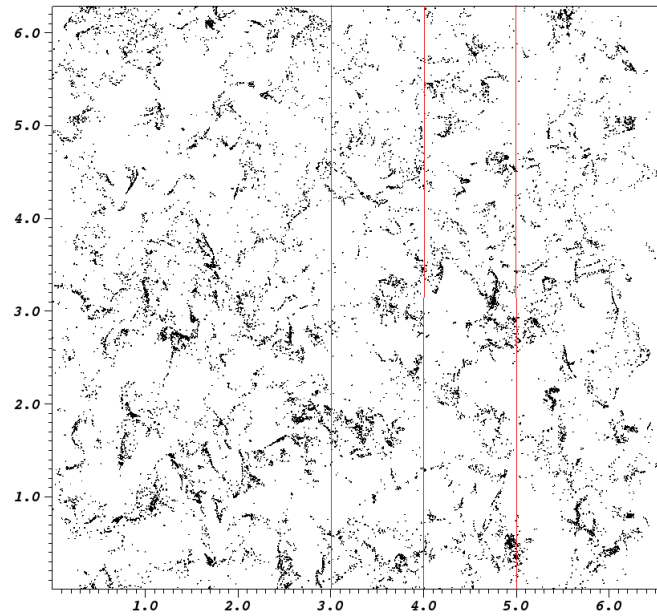


(a) Water droplets spatial distribution

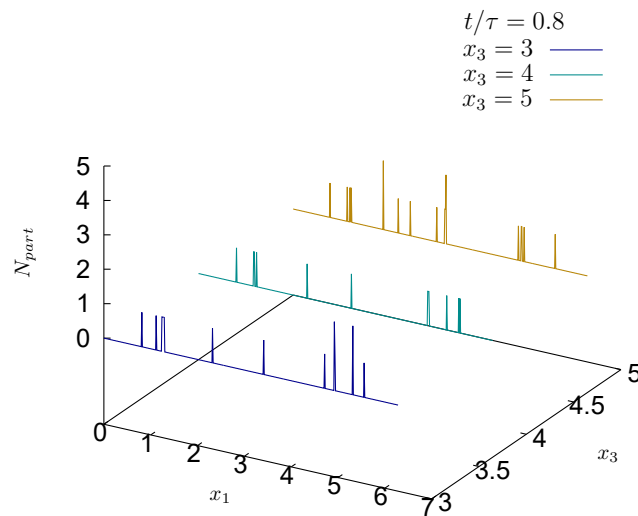


(b) Water droplets concentration

Figure 4.27. The figure (a) shows the water droplets spatial distribution at the initial condition  $t/\tau = 0$ , while the figure (b) shows the droplets concentration in direction  $x_1$  at three different positions along the inhomogeneous direction,  $x_3 = 3$ ,  $x_3 = 4$ ,  $x_3 = 5$  at the same time instant.

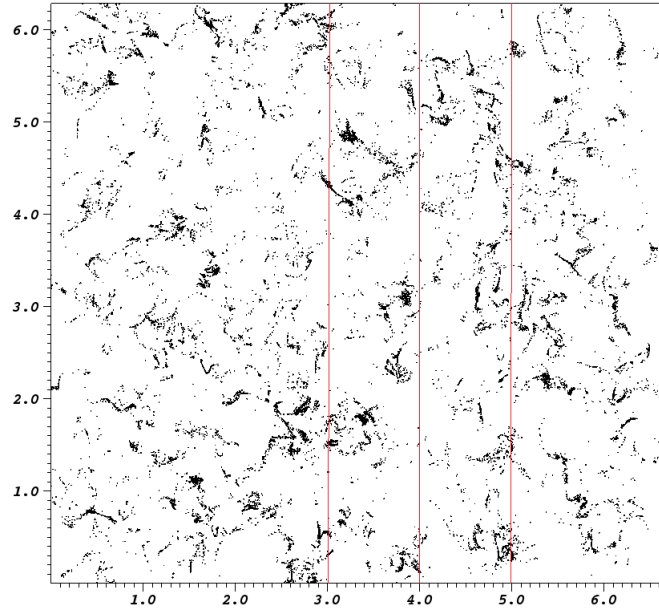


(a) Water droplets spatial distribution

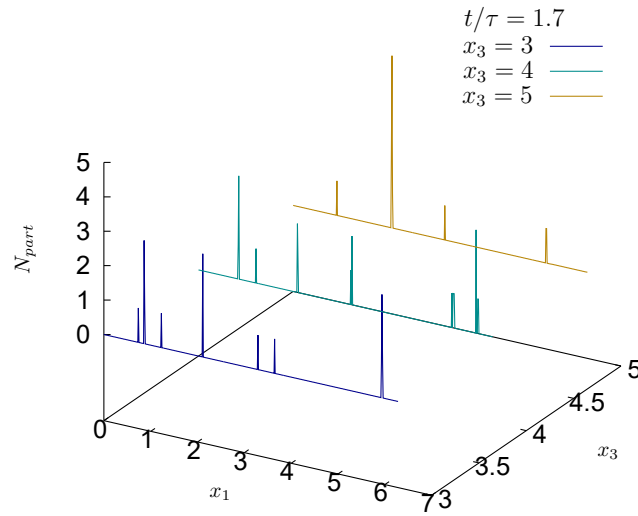


(b) Water droplets concentration

Figure 4.28. The figure (a) shows the water droplets spatial distribution at  $t/\tau = 0.8$ , while the figure (b) shows the droplets concentration in direction  $x_1$  at three different positions along the inhomogeneous direction,  $x_3 = 3$ ,  $x_3 = 4$ ,  $x_3 = 5$  at the same time instant.



(a) Water droplets spatial distribution



(b) Water droplets concentration

Figure 4.29. The figure (a) shows the water droplets spatial distribution at  $t/\tau = 1.7$ , while the figure (b) shows the droplets concentration in direction  $x_1$  at three different positions along the inhomogeneous direction,  $x_3 = 3$ ,  $x_3 = 4$ ,  $x_3 = 5$  at the same time instant.

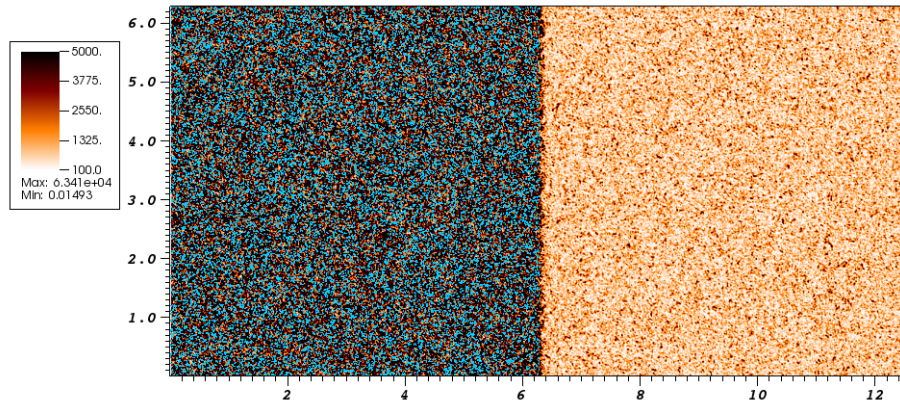
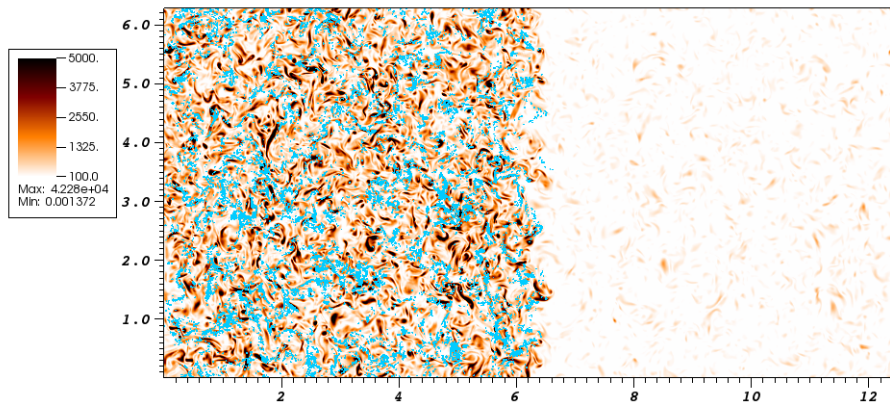
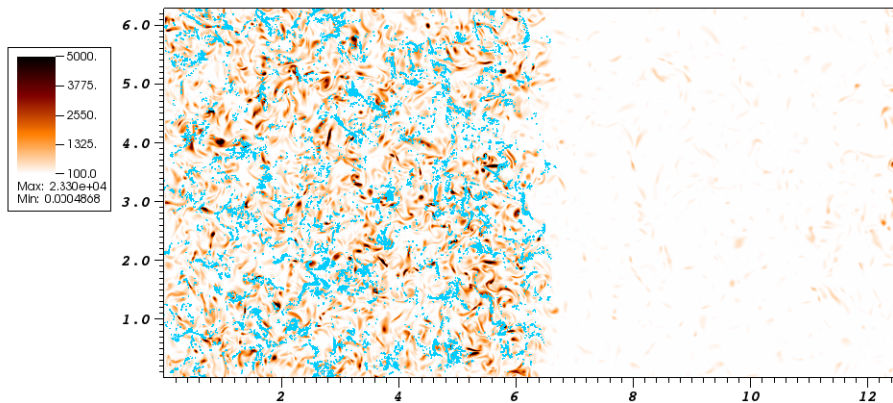
(a)  $t/\tau = 0$ (b)  $t/\tau = 0.8$ (c)  $t/\tau = 1.7$ 

Figure 4.30. In the figure the overlapping of the water droplets spatial distribution on the enstrophy flow is shown, for the supersaturated case, at three time instants,  $t/\tau = 0$  (a),  $t/\tau = 0.8$  (b) and  $t/\tau = 1.7$  (c). Data obtained for a Taylor microscale Reynolds number  $Re_\lambda = 43$ .

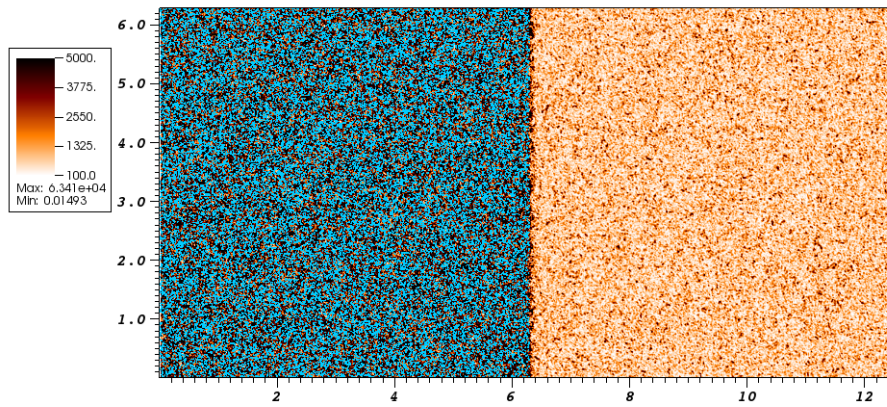
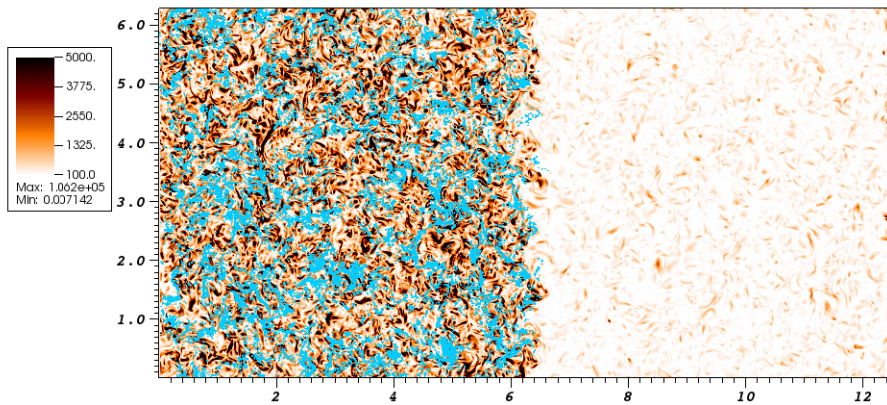
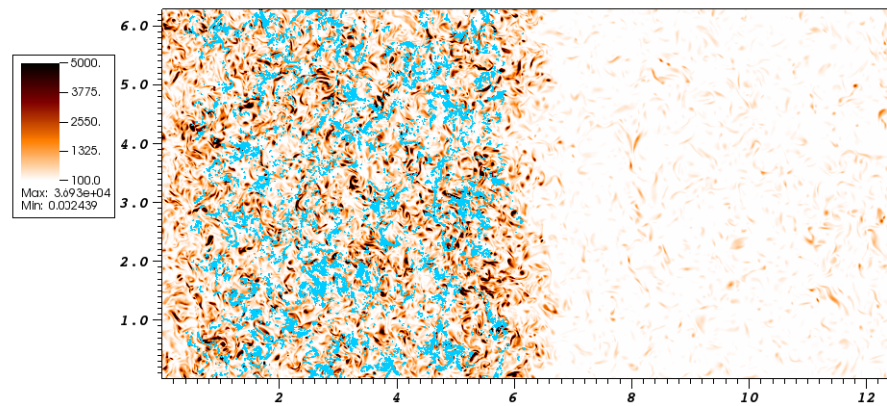
(a)  $t/\tau = 0$ (b)  $t/\tau = 0.8$ (c)  $t/\tau = 1.7$ 

Figure 4.31. In the figure the overlapping of the water droplets spatial distribution on the enstrophy flow is shown, for the supersaturated case, at three time instants,  $t/\tau = 0$  (a),  $t/\tau = 0.8$  (b) and  $t/\tau = 1.7$  (c). Data obtained for a Taylor microscale Reynolds number  $Re_\lambda = 53$ .

# Chapter 5

## Conclusions

A simplified cloud-clear air interface is analysed through a DNS code. Two simulations have been carried out which analyse one the supersaturate case and the other the saturate case. In both cases the number of time steps is 6500, which gives for a  $\Delta\tilde{t} = 10^{-4}$ , a total time simulated of  $t = 1.7\tau$  where  $\tau$  is the eddy turnover time relative to the eddy whose scale is equal to the integral length scale. According to [Vaillancourt & Yau \(2000\)](#) the initial distribution of water droplets causes large supersaturation fluctuations, this can explain the strong asymmetry in the temperature and water vapour density skewness and kurtosis for the supersaturate case (see figures [4.17](#) and [4.16](#)). The time simulated is too low in order to appreciate an important widening of the mixing layer and a significant entrainment of the clear air inside the cloud region. Some effects of the entrainment, albeit small, can be seen in the total volume distribution in the inhomogeneous direction for the saturate case and supersaturated case (see figure [4.21](#) (b)) where the entrainment of subsaturate clear air cause the particles to evaporate and the volume distribution profile to shrink. Another important result is the slight broadening of the droplet size spectrum. In real cloud a very large broadening of the droplets size spectrum was observed. The broadening of the droplet spectrum according to [Chandrakar \*et al.\* \(2016\)](#) is related to the initial aerosol concentration and it depends on the supersaturation fluctuations. As already mentioned, in our work the time simulated is too short to appreciate a significant size distribution broadening, but it can be seen that in the saturate case all the particles undergo a strong evaporation till the mean droplet radius reaches  $0.2R_{in}$  after  $1.7\tau$ , while the opposite trend is shown in the supersaturate case, where the condensation allows the particles to grow and the mean droplet radius after the same time is  $1.4R_{in}$ . Despite the short time simulation, it can be seen in the droplets size distribution spectrum that the peak decrease with time, moving towards larger radius values (supersaturate case) or smaller values (saturate case) and

the distribution widens in both cases. In conclusion the clustering or preferential concentration is observed. A visualization of the enstrophy flow together with the spatial inertial particles distribution, shows how the water droplets concentrates in the low vorticity regions. In this work the nucleation has not been taken into account and an initial monodisperse homogeneous drops distribution is considered with an initial radius of  $2.5 \mu m$ . The water droplet growth is due mainly to the condensation process. The particles are too small for the collision-coalescence mechanism to be efficient. For future work, an initial monodisperse droplets distribution of radius larger than  $40 \mu m$  can be considered and the collision-coalescence growth mechanism can be investigated through the same DNS code and the resulting droplets size distributions can be analysed.

# Bibliography

- BEARD, KV & OCHS, HT 1993 Warm-rain initiation: an overview of microphysical mechanism. *F. Appl. Meteorol.* **32**, 608–25.
- BLYTH, A. M., COOPER, W. A. & JENSEN, J. B. 1988 A study of the source of entrained air in montana cumuli. *J. Atmos. Sci.* **45**, 3944–3964.
- CHANDRAKAR, KAMAL KANT, CANTRELL, WILL, CHANG, KELKEN, CIOCHETTO, DAVID, NIEDERMEIER, DENNIS, OVCHINNIKOV, MIKHAIL, SHAW, RAYMOND A. & YANG, FAN 2016 Aerosol indirect effect from turbulence-induced broadening of cloud-droplet size distributions. *PNAS* **113** (50), 14243–14248.
- DEVENISH, B. J., BARTELLO, P., BRENGUIER, J. L., COLLINS, L. R., GRABOWSKI, W. W., IJZERMANS, R. H. A., MALINOWSKI, S. P., REEKS, M. W., VASSILICOS, J. C., WANG, L. P. & WARHAFT, Z. 2012 Droplet growth in warm turbulent clouds. *Quarterly Journal of the Royal Meteorological Society* **138**, 1401–1429.
- GALLANA, L., SAVINO, S. DI, SANTI, F. DE, IOVIENO, M. & TORDELLA, D. 2014 Energy and water vapor transport across a simplified cloud-clear air interface. *J. Phys.: Conf. Series* **547** (1), 012042.
- GERBER, H., FRICK, G., MALINOWSKI, S. P., BRENGUIER, J-L. & BURNET, F. 2005 Holes and entrainment in stratocumulus. *J. Atmos. Sci.* **62**, 443–459.
- GERBER, H. E., FRICK, G. M., JENSEN, J. B. & HUDSON, J. G. 2008 Entrainment, mixing, and microphysics in trade-wind cumulus. *Journal of the Meteorological Society of Japan* **86A**, 87–106.
- GOTOH, TOSHIYUKI, SUEHIRO, TAMOTSU & SAITO, IZUMI 2016 Continuous growth of cloud droplets in cumulus cloud. *New Journal of Physics* **18**.
- GRABOWSKI, WOJCIECH W. & WANG, LIAN-PING 2013 Growth of cloud droplets in a turbulent environment. *Annual Review of Fluid Mechanics* **45**, 293–324.
- HEUS, T., VAN DIJK, G., JONKER, H. J. J. & VAN DEN AKKER, H. E. A. 2008 Mixing in shallow cumulus studied by lagrangian particle tracking. *J. Atmos. Sci.* **65**, 2581–2597.

- HEUS, T. & JONKER, H. J. J. 2008 Subsiding shells around shallow cumulus clouds. *J. Atmos. Sci.* **65**, 1003–1018.
- IOVIENO, MICHELE, CAVAZZONI, CARLO & TORDELLA, DANIELA 2001 A new technique for a parallel dealiased pseudospectral navier-stokes code. *Computer Physics Communications* **141**, 365–374.
- IOVIENO, M., SAVINO, S. DI, GALLANA, L. & TORDELLA, D. 2014 Mixing of a passive scalar across a thin shearless layer: concentration of intermittency on the sides of the turbulent interface. *Journal of Turbulence* **15** (5), 311–334.
- KUMAR, B., SCHUMACHER, J. & SHAW, R. A. 2013 Cloud microphysical effects of turbulent mixing and entrainment. *Theoretical and Computational Fluid Dynamics* **27**, 361–376.
- LAU, KM & WU, H-T 2003 Warm rain process over tropical oceans and climate implications. *Geophys. Res. Lett.* **30**, 2290.
- MACPHERSON, J. I. & ISAAC, G. A. 1977 Turbulent characteristics of some canadian cumulus clouds. *Journal of Applied Meteorology and Climatology* **16**, 81–90.
- MALINOWSKI, S. P., GERBER, H., PLANTE, I. JEN-LA, KOPEC, M. K., KUMALA, W., NUROWSKA, K., CHUANG, P. Y., KHELIF, D. & HAMAN, K. E. 2013 Physics of stratocumulus top (post): turbulent mixing across capping inversion. *Atmospheric Chemistry and Physics* .
- MAXEY, M. R. 1987 The gravitational settling of aerosol particles in homogeneous turbulence and random flow fields. *J. Fluid Mech.* **174**, 441–465.
- PAOLI, R. & SHARIFF, K. 2009 Turbulent condensation of droplets: direct simulation and a stochastic model. *F. Atmos. Sci.* **66**, 723–40.
- PHILOFLUID 2016 Collision detection algorithm. <https://areweb.polito.it/ricerca/philofluid/software/252-collision>, accessed: 2018-03-09.
- POPE, STEPHEN B. 2000 *Turbulent flows*, chap. 9. Cambridge University Press.
- PRUPPACHER, H. R. & KLETT, J. D. 1997 *Microphysics of clouds and precipitation*. Dordrecht: Kluwer Acad.
- RAES, F. 2006 Take a glass of water: concepts from physical chemistry used in describing the behaviour of aerosol and cloud droplets. *F. Phys. IV* **139**, 63–80.
- DE ROOY, WIM C., BECHTOLD, PETER, HILCH, KRISTINA FRÖ, HOHENEGGER, CATHY, JONKER, HARM, MIRONOV, DIMITRII, SIEBESMA, A. PIER, TEIXEIRA, JOAO & YANO, JUN-ICHI 2013 Entrainment and detrainment in cumulus convection: an overview. *Quarterly Journal of the Royal Meteorological Society* **139**, 1–19.

- SHAW, R. A. 2003 Particle-turbulence interactions in atmospheric clouds. *Ann. Rev. Fluid Mech.* **35**, 183–227.
- SHAW, R. A., READE, W. C., COLLINS, L. R. & VERLINDE, J. 1998 Preferential concentration of cloud droplets by turbulence: effects on the early evolution of cumulus cloud droplet spectra. *J. Atmos. Sci.* **55**, 1965–1976.
- SIDIN, R. S. R., IJZERMANS, R. H. A. & REEKS, M. W. 2009 A lagrangian approach to droplet condensation in atmospheric clouds. *Phys. Fluids* **21**, 106603.
- SIEBERT, H., LEHMANN, K. & WENDISCH, M. 2006 Observations of small-scale turbulence and energy dissipation rates in the cloudy boundary layer. *Journal of the Atmospheric Sciences* **63**, 1451–1466.
- SIEBERT, H., SHAW, R. A. & WARHAFT, Z. 2010 Statistics of small-scale velocity fluctuation and internal intermittency in marine stratocumulus clouds. *Journal of the Atmospheric Sciences* **67**, 262–273.
- SQUIRES, P. 1958 Penetrative downdraughts in cumuli. *Tellus* **10**, 381–389.
- STEVENS, BJORN 2005 Atmospheric moist convection. *Annual Review of Earth and Planetary Sciences* **33**, 605–43.
- TORDELLA, D. & IOVIENO, M. 2006 Numerical experiments on the intermediate asymptotics of shear-free turbulent transport and diffusion. *Journal of Fluid Mechanics* **549**, 429–441.
- TORDELLA, DANIELA & IOVIENO, MICHELE 2011 Small-scale anisotropy in turbulent shearless mixing. *Physical Review Letters* **107**, 194501.
- TORDELLA, DANIELA, IOVIENO, MICHELE & BAILEY, PETER ROGER 2008 Sufficient condition for gaussian departure in turbulence. *Physical Review E* **77**, 016309.
- TRITTON, D. J. 1988 *Physical Fluid Dynamics*, chap. 14. Oxford:Oxford Science Publications.
- VAILLANCOURT, P. A. & YAU, M. K. 2000 Review of particle-turbulence interactions and consequences for cloud physics. *Bull. Am. Meteorol. Soc.* **81**, 285–298.
- VAILLANCOURT, P. A., YAU, M. K., BARTELLO, P. & GRABOWSKI, W. W. 2002 Microscopic approach to cloud droplet growth by condensation. part ii: Turbulence, clustering and condensational growth. *J. Atmos. Sci.* **59**, 3421–3435.
- VAILLANCOURT, P. A., YAU, M. K. & GRABOWSKI, W. W. 2001 Microscopic approach to cloud droplet growth by condensation. part i: Model description and results without turbulence. *Journal of the Atmospheric Sciences* **58**, 1945–64.

BIBLIOGRAPHY

---

- VOHL, O., MITRA, S. K., WURZLER, S. C. & PRUPPACHER, H. R. 1999 A wind tunnel study of the effects of turbulence on the growth of cloud drops by collision and coalescence. *J. Atmos. Sci.* **56**, 4088–4099.